Objective Diagnostics and the Madden–Julian Oscillation. Part II: Application to Moist Static Energy and Moisture Budgets

BRANDON O. WOLDING AND ERIC D. MALONEY

Department of Atmospheric Science, Colorado State University, Fort Collins, Colorado

(Manuscript received 10 October 2014, in final form 7 July 2015)

ABSTRACT

Processes controlling moisture variations associated with the MJO are investigated using budgets of moist static energy (MSE) and moisture. To first order, precipitation anomalies are maintained by anomalous large-scale vertical moisture advection, which can be understood through application of a weak temperature gradient balance framework to the MSE budget. Intraseasonal variations in longwave radiative cooling play a crucial role in destabilizing the MJO by enhancing intraseasonal variations in large-scale vertical moisture advection. This enhancement allows the effect of intraseasonal variations in large-scale vertical moisture advection to meet or exceed the effect of intraseasonal variations in net condensation, resulting in a positive feedback between the net effect of these processes and moisture anomalies. Intraseasonal variations in surface latent heat flux (SLHF) enhance this positive feedback, but appear to be insufficient to destabilize the MJO in the absence of radiative feedbacks.

The effect an ensemble cloud population has on large-scale moisture is investigated using fields where only high-frequency variability has been removed. During the enhanced phase, approximately 85% of the moisture removed by net condensation is resupplied by the large-scale vertical moisture advection associated with apparent heating by microphysical processes and subgrid-scale vertical fluxes of dry static energy. This suggests that a relatively large increase in net condensation could be supported by a relatively small anomalous moisture source, even in the absence of radiative feedbacks. These results highlight the importance of process-oriented assessment of MJO-like variability within models, and suggest that a weak temperature gradient (WTG) balance framework may be used to identify destabilization mechanisms, thereby distinguishing between MJO-like variability of fundamentally different character.

1. Introduction

Variability in the tropical atmosphere on time scales less than a season is strongly influenced by the Madden–Julian oscillation (MJO), a phenomena traditionally described as a large-scale coupling of deep convection and tropospheric circulation anomalies that propagates eastward at approximately $5\,\mathrm{m\,s^{-1}}$. Since its discovery over four decades ago (Madden and Julian 1971), tremendous effort has been put into explaining the existence of the MJO and improving its representation in models. This effort is warranted by the MJO's far-reaching societal impacts, which result from its direct impacts as well as its interactions with phenomena such as tropical cyclone activity (Maloney and Hartmann 2000a,b; Hall et al. 2001; Slade and Maloney 2013) and interannual variability (McPhaden 1999; Takayabu et al. 1999). Despite continual advancement in the understanding of the MJO, various observed features remain insufficiently explained by the physical mechanisms proposed to be responsible for the MJO's existence. Zhang (2005) and Wang (2012) provide a good overview of this body of work.

The development of large-scale regions of anomalous free-tropospheric humidity has played a central role in several recent theories of the MJO, including discharge–recharge theory (Bladé and Hartmann 1993; Hu and Randall 1994; Benedict and Randall 2007), multiscale theories (Majda and Stechmann 2009, 2011), and moisture-mode theory (Sobel et al. 2001; Raymond and Fuchs 2009; Sobel and Maloney 2012, 2013). A moist free troposphere can promote convection by reducing the diminishment of buoyancy that occurs as a rising plume entrains environmental air, and by reducing penetrative downdrafts that lower boundary layer θ_e and potentially inhibit further convection (Raymond 1995).

Corresponding author address: Brandon Wolding, Department of Atmospheric Science, Colorado State University, 200 W. Lake St., 1371 Campus Delivery, Fort Collins, CO 80523-1371.
E-mail: brandon.wolding@gmail.com

DOI: 10.1175/JCLI-D-14-00689.1

The former is particularly important to convection over tropical oceans, where observations indicate that large dilution of updrafts occurs below 500 hPa (Lucas et al. 1994; Zipser 2003). The influence of moisture on tropical convection is enhanced by the small Coriolis parameter of the tropics, which allows gravity waves to quickly disperse buoyancy anomalies over large horizontal distances, making the realization of free-tropospheric temperature anomalies on larger spatiotemporal scales difficult (Charney 1963; Maloney and Sobel 2007; Yano and Bonazzola 2009). Peters and Neelin (2006) used observations to show that the transition to deep convection occurs at a critical column water vapor (CWV), and Neelin et al. (2009) showed that precipitation statistics for different temperature regimes collapse to a simple dependence on CWV and critical CWV when vertically averaged tropospheric temperature is taken into account. Sahany et al. (2012) found that lower free-tropospheric moisture was particularly important, highlighting potential ''choke points'' where dry air entrainment could prevent a plume from undergoing deep convection. While the interaction between free-tropospheric humidity and convection is fundamental to both discharge–recharge theory and moisture-mode theory, these theories differ significantly in their view of the mechanisms controlling free-tropospheric humidity and the manner in which anomalous convection and moisture interact.

Although not originally conceptualized in terms of free-tropospheric humidity (Hu and Randall 1994), the discharge–recharge framework has been applied by studies that have observed an extended ''recharge'' period of gradual tropospheric moistening preceding MJO convective events, which subsequently ''discharge'' moisture during periods of enhanced convection (Bladé and Hartmann 1993; Kemball-Cook and Weare 2001; Kiladis et al. 2005; Benedict and Randall 2007; Thayer-Calder and Randall 2009). In this view, processes act to moisten the lower free troposphere during convectively quiescent periods, reducing the effects of dry air entrainment and eventually making the environment favorable for the onset of deep convection. The onset of deep convection is responsible for the discharge of free-tropospheric moisture and the return to quiescent conditions. In other words, suppressed convective conditions push the system toward enhanced convective conditions, and vice versa. The processes that recharge moisture must be favored east of the regions that discharge moisture in order to drive propagation, and the time period required for processes to discharge and recharge free-tropospheric moisture determines the overall period of the oscillation.

Moisture-mode theory (Sobel et al. 2001; Raymond 2001) seeks to explain the MJO using a simplified set of equations, whereby horizontal temperature gradients and temperature tendency are neglected under weak temperature gradient (WTG) balance. The distribution of convection is diagnosed from that of moisture, which is prognostically determined. Instability of the moisture mode occurs if a feedback exists such that convection, acting through various processes, results in a further enhancement of moisture anomalies. Of particular relevance to this study is the work of Chikira (2014), who showed the net effect of vertical advection and cloud processes (termed the ''column process'') worked as a positive feedback to positive moisture anomalies in the enhanced phase of the MJO in both model results and European Centre for Medium-Range Weather Forecasts (ECMWF) interim reanalysis (ERA-Interim). Using a novel method of assessing the moisture budget of the model MJO, Chikira (2014) provided a unique insight as to what mechanisms may be responsible for this instability. Invoking WTG balance, the prognostic equations of potential temperature and free-tropospheric moisture were linked, allowing diabatic processes to be directly related to environmental vertical motion. The large-scale vertical motion associated with various diabatic processes was assessed, and the resulting vertical moisture advection quantified. The reduction of radiative cooling (which is associated with a reduction in large-scale subsidence under WTG balance) in the enhanced phase of the model MJO was shown to be the primary driver of anomalous lower free-tropospheric moistening. Janiga and Zhang (2015, manuscript submitted to *J. Atmos. Sci.*, hereinafter JZ) applied a similar theoretical framework to a cloud-permitting model simulation of an MJO event that occurred during the Dynamics of the Madden–Julian Oscillation (DYNAMO) field campaign, and also found that the reduction of longwave radiative cooling helped to maintain moisture anomalies during the enhanced phase. While moisture-mode theory and discharge–recharge theory are compatible in many ways, the results of Chikira (2014) and JZ suggest that instead of acting to discharge moisture anomalies and stabilize the atmosphere, the ensemble cloud population present during the enhanced phase of the MJO helps support moisture anomalies against the drying effect of horizontal advection, thereby helping maintain atmospheric instability.

Many other attempts have been made to understand the mechanisms controlling moisture variations associated with the MJO (Benedict and Randall 2007; Maloney 2009; Maloney et al. 2010; Kiranmayi and Maloney 2011; Andersen and Kuang 2012; Wu and Deng 2013; Kim et al. 2014a). Efforts using moisture budgets (Kiranmayi and Maloney 2011), particularly in

the enhanced phase of the MJO, are often stymied by the difficult task of quantifying the small moisture tendency that results from large anomalous moistening due to vertical moisture advection and large anomalous drying due to processes associated with deep convection (e.g., precipitation). The small moisture tendency that results from these large processes is key to understanding moisture variations associated with MJO, and distinguishing between a discharge–recharge mechanism and certain moisture-mode mechanisms for the MJO. An alternative approach to assessing the small residual moistening tendency is the use of a vertically integrated moist static energy (MSE) budget (Maloney 2009; Maloney et al. 2010; Kiranmayi and Maloney 2011; Andersen and Kuang 2012; Wu and Deng 2013; Kim et al. 2014a; Sobel et al. 2014). In addition to providing insight into the role of various diabatic processes (e.g., radiative heating) whose importance has been highlighted in recent studies (Chikira 2014; JZ; Yokoi 2015), use of the column MSE budget has the benefit of allowing the net effect of large-scale vertical moisture advection and precipitation on column moisture content to be assessed without having to directly quantify precipitation. Note that while MSE remains unchanged by latent heat release associated with vapor–liquid transitions, MSE is not conserved during liquid–ice transitions. While use of a column-integrated approach makes the assessment of moisture and MSE budgets of the MJO more tractable, it is worth highlighting that important information about the vertical structure of the physical processes at work cannot be determined using this approach alone (Matthews 2008; Ling et al. 2013; Chikira 2014).

While these studies have provided a great deal of insight into systematic variations of moisture associated with the MJO, documentation of the mechanisms responsible for these variations remains relatively incomplete. The limited geographical scope of many of these studies, and their focus on the enhanced phase of the MJO, brings into question how ''systematic'' of a role various mechanisms play. This study compares anomalous column moisture and MSE budgets of the MJO, and uses methods introduced in Wolding and Maloney 2015, hereinafter Part I) to assess the geographical variability of their various terms. The residual of each budget is presented, and implications for the interpretation of mechanisms responsible for moisture variations associated with the MJO discussed. A theoretical framework similar to that implemented by Chikira (2014) and JZ is applied to ERA-Interim for the first time. Processes responsible for intraseasonal variations in large-scale vertical moisture advection are investigated using vertical profiles of various apparent heating (Yanai et al. 1973) processes. Finally, the column moisture budget is used to examine the role of various processes in destabilizing the MJO.

Section 2 discusses the various datasets utilized in this study, calculation of the anomalous MSE and moisture budgets, and methods used in composite analysis. Results and discussion of both budgets are presented in section 3, as well as further interpretation of the MSE budget in the context of WTG balance. Summary and conclusions of this study are presented in section 4.

2. Data and methodology

Moisture and MSE budgets are calculated using ERA-Interim (Dee et al. 2011), provided by the ECMWF. The data were obtained every 6-h at a 1.5° × 1.5° resolution for the years 1979–2012. Unless otherwise indicated, the various terms of the budget (tendencies, horizontal advection, etc.) were calculated from the 6-hourly data, vertically integrated from the surface to 100 hPa, and then averaged to daily. ERA-Interim apparent and radiative heating rates were obtained directly from the ECMWF. Please note that ERA-Interim precipitation was used in the calculation of the moisture budget. Daily 2.5° × 2.5° NOAA interpolated OLR (Liebmann and Smith 1996) was similarly obtained for the years 1979–2012. Both aforementioned datasets were either low-pass or bandpass filtered to various time scales as indicated in text and figures, and then limited to boreal winter months (October–April) from 1 October 1980 to 30 April 2011 before compositing. In all figures presented in this study, terms that have been low-pass filtered to 20 or 100 days are indicated by subscripts of LP20 and LP100, respectively, while terms that have been bandpass filtered to 20–100 days are indicated by the subscript MJO. TRMM 3B42 dataset daily precipitation was obtained every 3 h at 0.25° × 0.25° resolution, averaged to daily resolution, bandpass filtered to 20–100 days, and then limited to boreal winter months from 1 October 1999 to 30 April 2011.

Composite analysis is performed using the filtered MJO OLR (FMO) index (Kiladis et al. 2014). (The FMO index and the EOFs used in its calculation can be obtained from http://www.esrl.noaa.gov/psd/mjo/mjoindex/.) To match the phase convention of the real-time multivariate MJO (RMM) index (Wheeler and Hendon 2004), EOF1 and PC1 were multiplied by −1, and then the order of the first two EOFs and principal components (PCs) was reversed. This was motivated by the widespread use of the RMM index, its potential familiarity to the reader, and because this convention was also adopted by Kiladis et al. (2014). Composites are made using the relative phase, a diagnostic

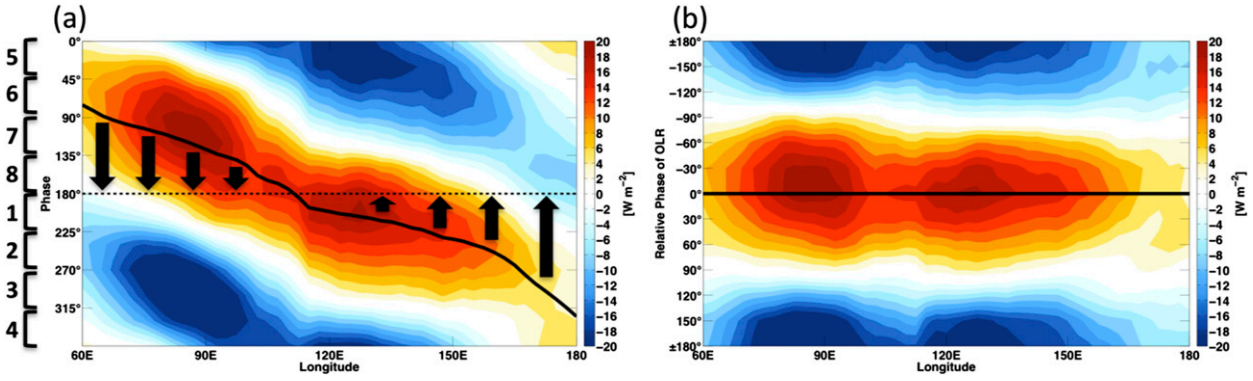

FIG. 1. Figure 7 from Part I. Composite of latitudinally averaged (15°N–15°S) NOAA OLR anomalies (shading) as a function of (a) phase of the FMO index and (b) relative phase of OLR in the FMO index. Days when the magnitude of the FMO index did not exceed a value of 1 were excluded. Latitudinally averaged OLR anomalies were binned by (a) phase and (b) relative phase, with bins spanning 60° calculated every 30°. The solid black line is the grid point phase of OLR in the FMO index. The boldface numbers adjacent to the brackets in (a) indicate the corresponding RMM phase, as defined by Wheeler and Hendon (2004). The block arrows indicate how the data are "shifted" in the transition from (a) to (b). In (b), moving downward from the top of the figure corresponds with the transition from enhanced convection (top of the figure, negative OLR anomalies) to suppressed convection (middle of the figure, positive OLR anomalies), and back to enhanced convection (bottom of the figure, negative OLR anomalies) at each longitude. Please note that subsequent plots are shifted such that the enhanced phase of the MJO is located in the center of the figure.

developed in Part I of this study. The relative phase objectively identifies the index phase where the largest MJO-related anomalies in a given field are likely to be observed for a given geographical location. Figure 1a illustrates a traditional phase composite of latitudinally averaged NOAA OLR anomalies, where the boldface numbers adjacent to the brackets indicate the "phase" as defined by Wheeler and Hendon (2004). The black line in Fig. 1a indicates the objectively determined phase at which positive OLR anomalies are the largest at each longitude. Block arrows indicate the manner in which data are shifted in the transition from Figs. 1a to 1b, such that maximum OLR anomalies are now centered in Fig. 1b. Subsequent plots are shifted such that the enhanced phase of the MJO is located in the center of the figure. Further details of the relative phase, and its calculation, are given in Part I.

Data are composited as a function of relative phase of OLR for the FMO index. This is done by first restricting dates to periods when the magnitude of the respective index exceeded a value of 1. Data at each point are then binned by relative phase, with bins spanning 30° of relative phase made every 15°. The minimum number of days included in any single bin is 225 for composites spanning 1980–2011, and 60 for composites spanning 1999–2011. (Vertical profiles presented in Figs. 6–9 were composited in similar fashion, except spatially averaging was performed over the region 5°N–10°S, 75°–85°E. These figures will be discussed in the following section.)

Composite "snapshots" presented in Fig. 2 were produced by selecting days when the relative phase of OLR at 80°E was within 10° of ±180°. This corresponds to maximum negative OLR anomalies at 80°E, as seen halfway down the vertical axis at 80°E in each plot of Fig. 3. These days were then limited to those when the FMO magnitude exceeded 1. Figures 2 and 3 will be discussed in the following section.

3. Results and discussion

a. A moisture budget perspective of the MJO

1) MOISTURE BUDGET FRAMEWORK

Neglecting $-\nabla \cdot \overline{q'\mathbf{V}_h'}$, the apparent moisture sink Q_2 is

$$Q_2 \equiv -L_v\left(\frac{\partial \overline{q}}{\partial t} + \overline{\mathbf{V}}_h \cdot \nabla \overline{q} + \overline{\omega}\,\frac{\partial \overline{q}}{\partial p}\right) = -L_v\left(\overline{M} - \frac{\partial \overline{\omega' q'}}{\partial p}\right), \tag{1}$$

where the overbar and prime indicate the large-scale average of a quantity and deviations from the area average, respectively; $\mathbf{V}_h$ and ω are the horizontal and vertical winds, respectively; q is specific humidity; L_v is the latent heat of vaporization; and M is the moisture tendency due to microphysical processes. Vertical eddy fluxes of moisture ($-\partial\overline{\omega' q'}/\partial p$) primarily represent moistening by subgrid-scale cumulus convection (Yanai and Johnson 1993). Decomposing M into contributions from various microphysical processes gives

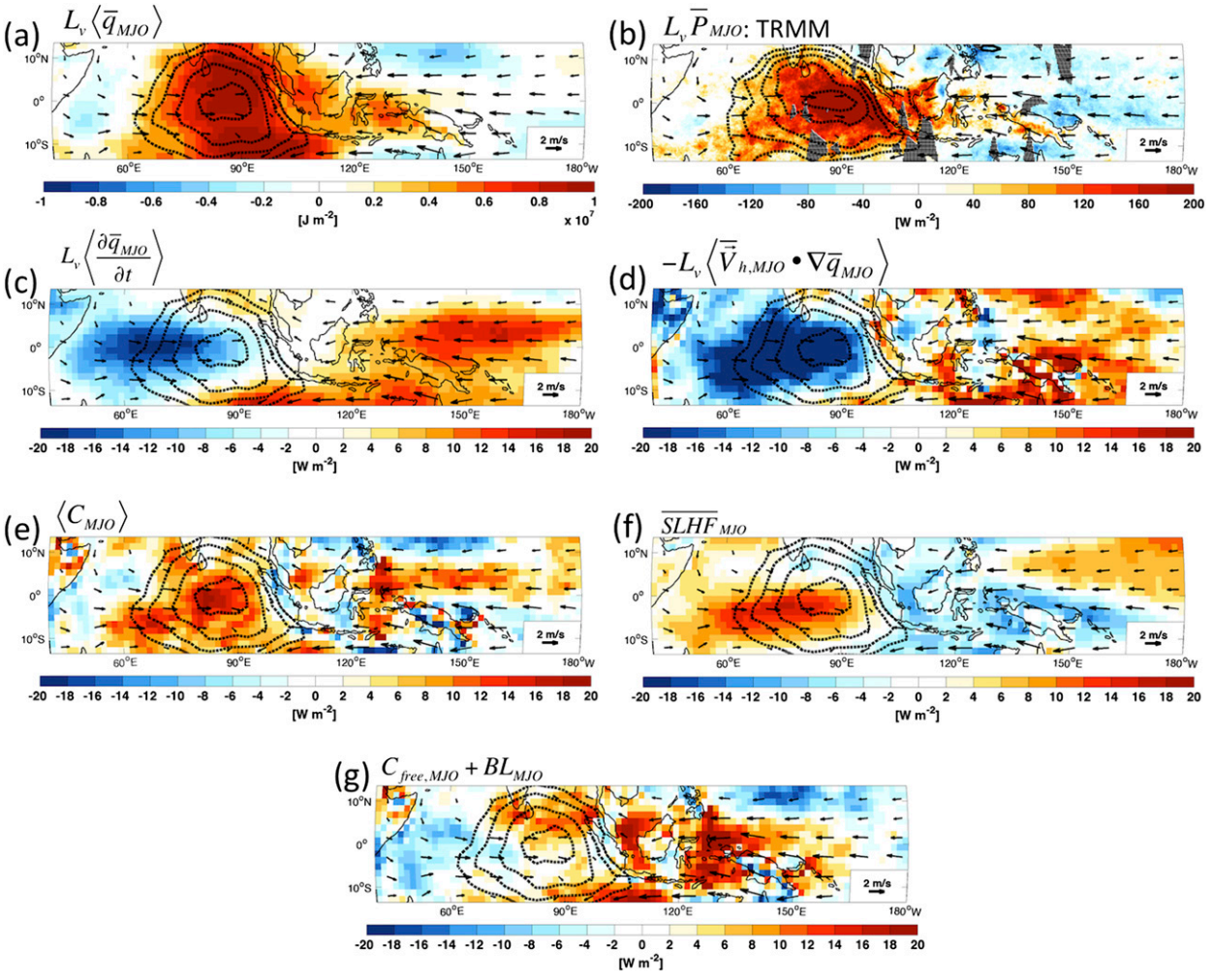

FIG. 2. Composite anomalies of (a) column specific humidity, (b)TRMM precipitation, (c) moisture tendency, (d) horizontal moisture advection, (e) column process, (f) SLHF, and (g) the sum of C_{free} and BL. Terms (a)–(e),(g) have been multiplied by the latent heat of vaporization. Solid (dashed) contours correspond to positive (negative) NOAA OLR anomalies every 5 W m^{-2} beginning at ±15 W m^{-2}. Arrows indicate ERA-Interim 850-hPa horizontal wind anomalies, and a reference arrow is provided in the lower-right corner. Please note that composites (a) and (c)–(h) result from 75 independent events for 1980–2011, while composite (b) results from 28 events for 1999–2011, and that the color bar in (b) spans from −200 to 200 W m^{-2}. Stippling in (b) indicates missing TRMM data. The subscript MJO indicates bandpass filtering to 20–100 days. See text for description of compositing technique.

$$M = -\frac{1}{L_v} Q_{\text{ce}} - \frac{1}{L_s} Q_{\text{ds}}, \tag{2}$$

where Q_{ce} and Q_{ds} are the dry static energy (DSE) tendency due to condensation minus evaporation (hereafter net condensation) and deposition minus sublimation (hereafter net deposition), respectively, and L_s is the latent heat of sublimation. The Eulerian moisture tendency is obtained by rearranging Eq. (1), giving

$$\begin{aligned} \frac{\partial \overline{q}}{\partial t} &= -\overline{\mathbf{V}}_h \cdot \nabla \overline{q} - \overline{\omega} \frac{\partial \overline{q}}{\partial p} - \frac{1}{L_v} Q_2 \\ &= -\overline{\mathbf{V}}_h \cdot \nabla \overline{q} + C, \end{aligned} \tag{3}$$

where C is the column process introduced by Chikira (2014), which quantifies the moisture tendency resulting from large-scale vertical moisture advection, microphysical processes, and vertical eddy fluxes of moisture. In other words, C quantifies the moisture tendency resulting from all processes occurring within a vertical column with the exception of horizontal moisture advection. Integrating Eq. (3) through the depth of the troposphere gives

$$\left\langle \frac{\partial \overline{q}}{\partial t} \right\rangle = -\langle \overline{\mathbf{V}}_h \cdot \nabla \overline{q} \rangle + \langle C \rangle, \tag{4}$$

where

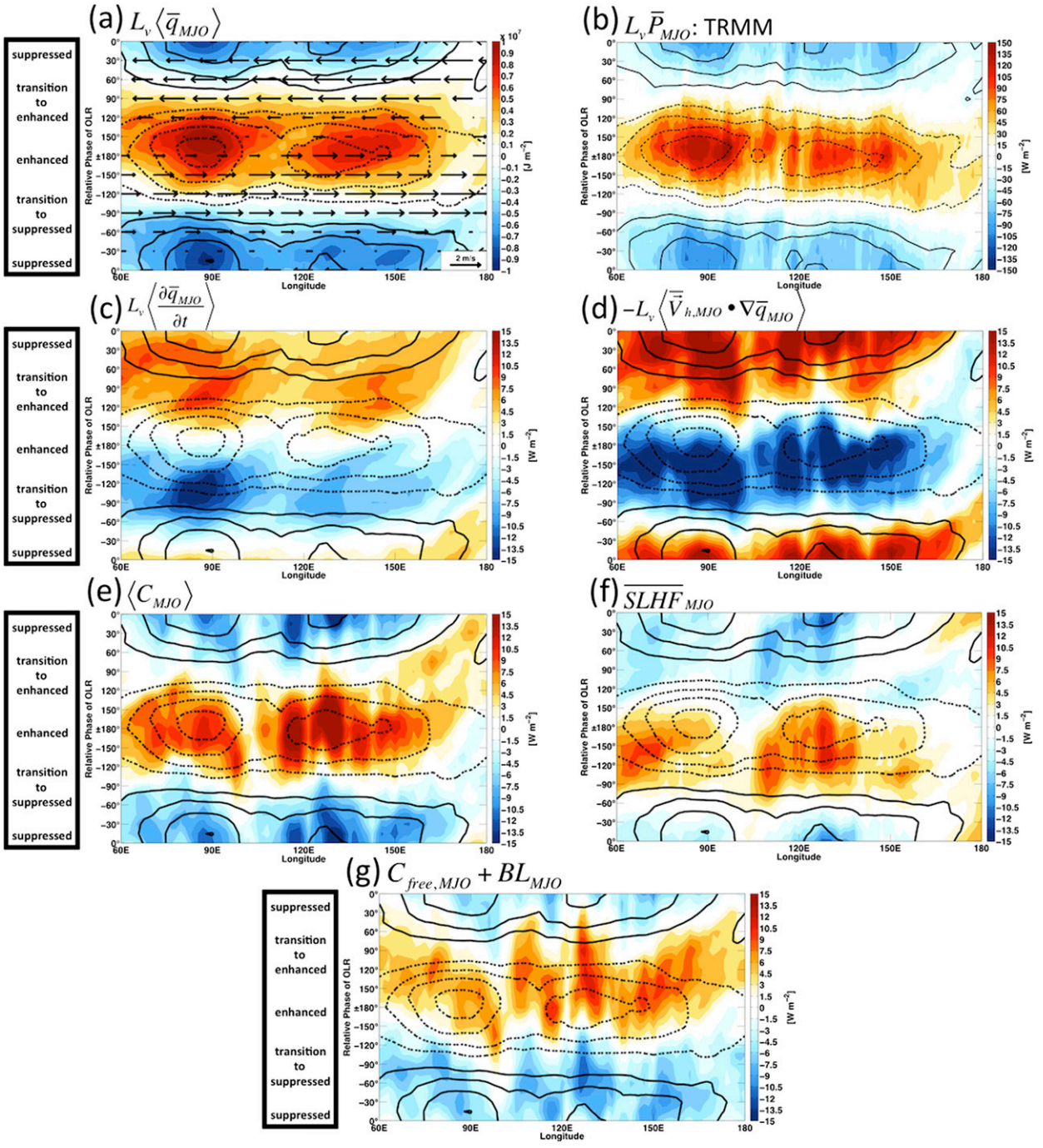

FIG. 3. Composite of (a) latitudinally averaged (13.5°N–13.5°S) ERA-Interim column latent heat, (b) TRMM precipitation, (c) column latent heat tendency, (d) column horizontal advection of latent heat, (e) column process, (f) SLHF, and (g) the sum of C_{free} and BL as a function of relative phase of OLR. Solid (dashed) contours correspond to positive (negative) NOAA OLR anomalies every 6 W m^{-2} beginning at ±6 W m^{-2}. Arrows in (a) indicate ERA-Interim U850 anomalies, and a reference arrow is provided in the lower-right corner. Moving downward from the top of the figure corresponds with the transition from suppressed convection (top of the figure, positive OLR anomalies) to enhanced convection (middle of the figure, negative OLR anomalies), and back to suppressed convection (bottom of the figure, positive OLR anomalies) at each longitude. The subscript MJO indicates bandpass filtering to 20–100 days. See text for description of compositing technique.

$$\langle C \rangle = C_{\text{free}} + \text{BL} + \frac{1}{L_v}\overline{\text{SLHF}}, \tag{5}$$

$$C_{\text{free}} = -\left\langle \overline{\omega}\,\frac{\partial \overline{q}}{\partial p} \right\rangle_{900} + \langle \overline{M} \rangle_{900}, \quad \text{and} \tag{6}$$

$$\text{BL} = -\left\langle \overline{\omega}\,\frac{\partial \overline{q}}{\partial p} \right\rangle_{1000}^{900} + \langle \overline{M} \rangle_{1000}^{900}, \tag{7}$$

and the angled brackets indicate the column integral from 1000 to 100 hPa; subscripts and superscripts on the angled brackets indicate differing lower and upper levels of integration, respectively; and SLHF is the surface flux of latent heat. The terms C_{free} and BL quantify the moisture tendency resulting from large-scale vertical moisture advection and microphysical processes within the free troposphere and boundary layer, respectively. In other words, the sum of C_{free} and BL quantifies the moisture tendency resulting from all processes occurring within a vertical column with the exception of fluxes of moisture from the surface and horizontal moisture advection. The distinction between C_{free} and BL is made because WTG balance, which is used in subsequent sections, is not applicable within the boundary layer, and because C_{free} is closely related to the aggregate effect an ensemble of clouds has on moisture (JZ). A detailed discussion of the physical processes controlling intraseasonal variations in C_{free} will be provided in a later section.

Please note that ERA-Interim does not provide the fields necessary to calculate $\overline{M}$, and that the approximation $\langle \overline{M} \rangle = \overline{P}$, where P is precipitation, was used in the actual calculation of the moisture budget. This approximation neglects the moisture tendency associated with net deposition and net condensation that does not result in precipitation. As will be discussed in subsequent sections, the inability to close the column moisture budget motivated the choice to calculate C as the residual of the moisture tendency and horizontal advection, and to calculate the sum of C_{free} and BL as the residual of the moisture tendency, horizontal advection, and SLHF. This choice was made because the moisture tendency, horizontal advection, and SLHF are likely better constrained within ERA-Interim than the remaining budget terms (e.g., precipitation). Calculated in this manner, C and the sum of C_{free} and BL should include representation of all process included in $\langle \overline{M} \rangle$.

2) The MJO in the eastern Indian Ocean

Before analyzing the geographical variability of processes affecting column moisture, we begin by looking at a composite "snapshot" of various processes when anomalous OLR is at a minimum at 80°E. Composite anomalies of column latent heat and the various terms in Eq. (4) are presented in Fig. 2. Please note that the subscript notation used in Fig. 2, as well as all subsequent figures, is defined in section 2 and within figure captions. Maximum column latent heat anomalies (Fig. 2a) of approximately $1 \times 10^7\,\text{J m}^{-2}$ (~4 mm) are approximately collocated with minimum OLR anomalies. Maximum TRMM precipitation anomalies (Fig. 2b) of approximately $200\,\text{W m}^{-2}$ (~7 mm day^{-1}) are also approximately collocated with minimum OLR anomalies. The distribution of TRMM precipitation anomalies closely matches the overall distribution of column latent heat anomalies, but has a clear maximum near the equator in comparison to the broader maximum of column latent heat anomalies. It is worth highlighting that, in the absence of anomalous moisture sources, anomalous precipitation in this region could remove the enhanced column moisture content (presumably built up over the previous 10–15 days) in less than 1 day. Yet the moisture tendency (Fig. 2c) over much of the eastern Indian Ocean is near zero or weakly negative, particularly in regions where the precipitation anomalies are largest. This collocation of maximum precipitation anomalies with near-zero column moisture tendency is consistent with previous work (Benedict and Randall 2007; Kiranmayi and Maloney 2011), and indicates that some other process or processes are acting to maintain enhanced column moisture content against dissipation by anomalous precipitation. These processes will now be identified.

The pattern of anomalous horizontal moisture advection (Fig. 2d) is very similar to that of the moisture tendency and is typically of larger magnitude, acting as an anomalous moisture source over a broad region east of the convective maximum, and as an anomalous moisture sink to the west where strong westerly 850-hPa zonal wind (U850) anomalies are evident. Worth noting is the extent to which anomalous horizontal advective drying extends through the region of minimum OLR anomalies, acting as an additional moisture sink in regions of strong precipitation and enhanced column moisture content. In contrast, C anomalies (Fig. 2e) have a distribution similar to both moisture and precipitation anomalies, helping to maintain column moisture anomalies against dissipation by enhanced precipitation. In other words, the net effect of anomalous SLHF, large-scale vertical moisture advection, and microphysical processes during the mature stage of the MJO is to further moisten the column. SLHF (Fig. 2f) is enhanced along a narrow strip of strong westerly U850 anomalies in the Indian Ocean, and suppressed over oceanic regions of the Maritime Continent where easterly U850 anomalies are present. While the enhancement of SLHF does contribute substantially to C

anomalies, they only provide 5%–10% of the moisture removed by anomalous precipitation in the eastern Indian Ocean. This is consistent with results obtained from buoy observations in the Indian Ocean by Riley-Dellaripa and Maloney (2015), and indicates that the vast majority of moisture removed by enhanced precipitation during the enhanced phase of the MJO is supplied by anomalous large-scale vertical moisture advection (i.e., horizontal convergence and divergence acting throughout the column). In fact, Fig. 2g shows that the sum of C_{free} and BL anomalies is near zero or weakly positive in the region of enhanced precipitation, suggesting that the moisture supplied by anomalous large-scale vertical moisture advection may actually exceed that removed by microphysical processes. The net effect of C_{free} and BL anomalies also appears to play an important role in moistening over the oceanic regions of the Maritime Continent to the east.

Taken together, the various processes presented in Fig. 2 are consistent with the findings of Chikira (2014) and Sobel et al. (2014), in that C anomalies are clearly acting to enhance column moisture anomalies. The role of anomalous horizontal moisture advection in both propagating column moisture anomalies eastward, as well as damping their further growth in the regions where precipitation anomalies are largest is qualitatively consistent with many previous studies (Benedict and Randall 2007; Kiranmayi and Maloney 2011; Sobel et al. 2014; Chikira 2014; Kim et al. 2014a). In considering the results of Fig. 2 presented above, it is important to remember that this is only a snapshot of the processes occurring when the MJO is at a given location. The extent to which these processes play an important role in other parts of the Eastern Hemisphere remains to be seen, as does the extent to which these processes are mirrored in the suppressed phase of the MJO.

3) The MJO in the Eastern Hemisphere

To assess how the processes affecting anomalous moisture change as the MJO moves across the Eastern Hemisphere, relative phase composites of the various column moisture budget terms [Eq. (4)] are now examined. Figure 3a shows latitudinally averaged moisture (color shading), OLR (contours), and U850 (arrows) anomalies throughout a composite convective life cycle of the MJO. Moving downward from the top of the figure corresponds with the transition from suppressed convection (top of the figure, positive OLR anomalies) to enhanced convection (middle of the figure, negative OLR anomalies), and back to suppressed convection (bottom of the figure, positive OLR anomalies) at each longitude. The transition from suppressed to enhanced convection is accompanied by easterly U850 anomalies, and the transition back to suppressed conditions is accompanied by westerly U850 anomalies. These basic features are consistent with the well-documented structure of the MJO (Madden and Julian 1972; Wheeler and Hendon 2004; Kiladis et al. 2005). Column moisture anomalies and TRMM precipitation anomalies (Fig. 3b) tend to peak between 15° and 30° of phase prior to OLR anomalies, which is approximately 1.5–3 days for a MJO event of typical duration. The tendency for OLR to be disproportionately influenced by widespread anvil decks that persist for considerable times (Morita et al. 2006) may explain this slight offset. While OLR is used as a convenient proxy for convection in this study, the interaction of various processes with column moisture is of real interest. Therefore, the slight lag should be kept in mind during the subsequent discussion.

Comparing Figs. 3a–g with Figs. 2a–g largely supports generalizing the results of the previous section to the rest of the Indian Ocean and Maritime Continent region. Irrespective of geographical location, and during both the enhanced and suppressed phase, the moisture tendency (Fig. 3c) is near zero when precipitation anomalies are largest. Please note that the color bar values in Fig. 3b are an order larger than those in Figs. 3c–g. Anomalous horizontal advective moistening (Fig. 3d) contributes to the buildup of enhanced moisture anomalies, while anomalous horizontal advective drying contributes to their depletion, consistent with previous studies (Benedict and Randall 2007; Kiranmayi and Maloney 2011; Chikira 2014; Kim et al. 2014a; Pritchard and Bretherton 2014). During both enhanced and suppressed periods, C acts to enhance moisture anomalies (Fig. 3a), lagging moisture anomalies slightly in the central Indian Ocean and being approximately in phase with moisture anomalies in the Maritime Continent region. There is a notable gap in C between 100° and 105°E, where the Malay Peninsula and Sumatra span much of the latitude range considered here. As C is often positive when the total tendency is zero, this implies that horizontal advection plays a role in damping the further growth of moisture anomalies when they are largest.

Both SLHF and the net effect of C_{free} and BL anomalies (Figs. 3f,g) make substantial contributions to C anomalies discussed above, with the former acting as an anomalous moisture source predominantly in the late stages of enhanced convection and the latter in the early stages of enhanced convection. Most importantly, Fig. 3g suggests that intraseasonal variations in the net effect of large-scale vertical moisture advection and microphysical processes (i.e., the sum of C_{free} and BL) play no role in the discharge of column moisture anomalies during the enhanced phase of the MJO, which

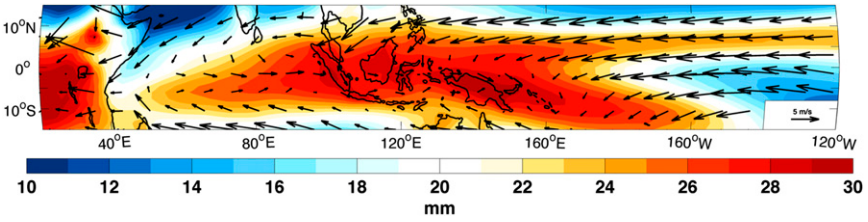

FIG. 4. ERA-Interim mean specific humidity integrated from 850 to 500 hPa (color contours) and 850-hPa horizontal wind for 1980–2011 winters (1 October–30 April). Reference wind vectors are provided in the lower-right corner of the panel.

appears to result entirely from the enhancement of horizontal advective drying. From the Indian Ocean to the eastern side of the Maritime Continent, latitudinally average SLHF is reduced during periods of easterly wind anomalies (when moisture anomalies are growing), and enhanced during period of westerly wind anomalies (when moisture anomalies are dissipating). The distribution of SLHF largely reflects the distribution of boreal winter mean low-level westerly winds (Fig. 4), which determines where wind anomalies associated with the MJO add constructively or destructively to mean winds (Shinoda et al. 1998; Riley-Dellaripa and Maloney 2015). The change in mean state winds that occurs east of the Maritime Continent explains the change in the SLHF anomalies that occurs in this region in Fig. 3f.

To summarize, the results of Fig. 3 suggest that the processes controlling column moisture variations associated with the MJO do not change as a function of geographical location throughout much of the Eastern Hemisphere. Figure 3 also shows that the processes controlling column moisture content in the enhanced phase are approximately mirrored in the suppressed phase. Column moisture content recharged in the weeks leading up to the onset of enhanced convection is insufficient to support prolonged enhanced precipitation during the enhanced phase of the MJO. To first order, prolonged enhanced precipitation is supported by the moisture supplied by anomalous large-scale vertical advection, which appears to actually exceed moisture removal by anomalous precipitation, resulting in a net moistening. At no point does the net effect of these processes appear to discharge column moisture anomalies.

4) A ROLE FOR THE MSE BUDGET

The results of this section have demonstrated that changes in horizontal advection and SLHF during the enhanced phase of the MJO are relatively modest, being a full order of magnitude smaller than changes in precipitation and large-scale vertical moisture advection, with the latter experiencing a threefold increase relative to climatological values in this region (not shown). Unfortunately, a moisture budget perspective alone does not provide much insight to the physical mechanisms that could be responsible for this dramatic change in large-scale vertical moisture advection. An even larger disadvantage of using a moisture budget alone to investigate the MJO is that the budget residual [i.e., the difference between the left- and right-hand sides of Eq. (3)] (Fig. 5a) is larger than the individual terms from which conclusions are often drawn. Accurate assessment of the small difference between the two large terms in C_{free} is important for distinguishing the role of various processes in destabilizing the MJO, as well as evaluating various theories of the MJO such as discharge–recharge theory and moisture-mode theory.

Fortunately the MSE budget offers solutions to both of these problems. Not only can the MSE budget be approximately closed, but recent studies (Chikira 2014; JZ) have begun developing a framework for using the MSE budget to understand the dramatic changes in large-scale vertical moisture advection. The next section will introduce the MSE budget, highlight the physical mechanisms that can drive changes in large-scale vertical moisture advection and C_{free}, and demonstrate that the conclusions drawn in this section are robust. Discussion of both the moisture budget and MSE budget residuals will be provided.

b. A MSE perspective of the MJO

1) MSE BUDGET FRAMEWORK

Moist static energy (h), DSE (s), and moisture are related by

$$h = s + L_v q. \tag{8}$$

Neglecting $-\nabla \cdot \overline{s'\mathbf{V}_h'}$, the apparent heat source Q_1 (Yanai et al. 1973) is

$$Q_1 \equiv \frac{\partial \overline{s}}{\partial t} + \overline{\mathbf{V}}_h \cdot \nabla \overline{s} + \overline{\omega}\frac{\partial \overline{s}}{\partial p} = \overline{Q}_s - \frac{\partial \overline{\omega' s'}}{\partial p}, \tag{9}$$

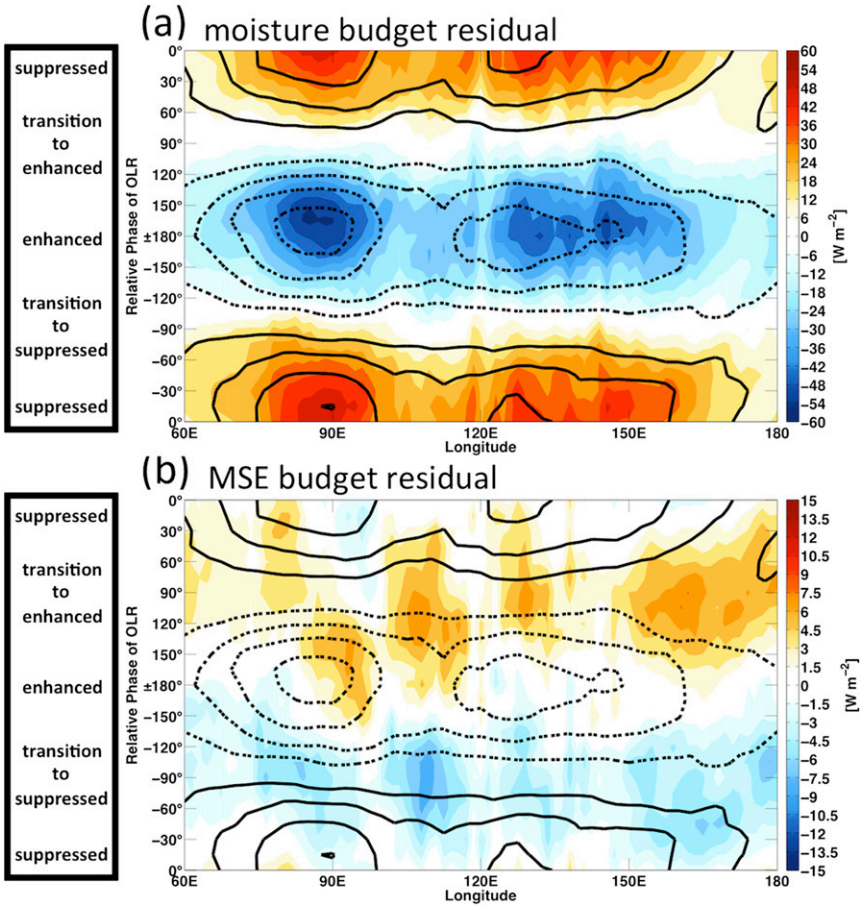

FIG. 5. As in Fig. 3, but color shading for (a) the moisture budget residual and (b) the MSE budget residual.

where Q_s is the DSE tendency due to diabatic processes. Vertical eddy fluxes of dry static energy ($-\partial\overline{\omega' s'}/\partial p$) primarily represent heating by subgrid-scale cumulus convection (Yanai and Johnson 1993). The DSE tendency due to diabatic processes results from latent heating associated with microphysical processes as well as radiative heating, such that

$$Q_s = Q_M + Q_R, \tag{10}$$

where Q_M and Q_R are the DSE tendency due to microphysics and radiation, respectively. Decomposing Q_M into contributions from various microphysical processes gives

$$Q_M = Q_{\text{ce}} + Q_{\text{fm}} + Q_{\text{ds}}, \tag{11}$$

where Q_{fm} is the DSE tendency due to net freezing minus melting.

Combining Eqs. (9) and (1) to arrive at the Eulerian MSE tendency gives

$$\begin{aligned}\frac{\partial \overline{h}}{\partial t} &= -\overline{\mathbf{V}}_h \cdot \nabla \overline{h} - \overline{\omega}\frac{\partial \overline{h}}{\partial p} + Q_1 + Q_2 \\ &= -\overline{\mathbf{V}}_h \cdot \nabla \overline{h} - \overline{\omega}\frac{\partial \overline{h}}{\partial p} + \overline{Q}_s + L_v \overline{M} - \frac{\partial \overline{\omega' s'}}{\partial p} - L_v \frac{\partial \overline{\omega' q'}}{\partial p}.\end{aligned} \tag{12}$$

This equation is our jumping off point for understanding variations in large-scale vertical moisture advection and C_{free} associated with the MJO.

2) MSE IN WTG BALANCE

In this section, WTG balance is used to understand variations in large-scale vertical moisture advection and C_{free}. The Eulerian tendency and horizontal advection of $\overline{s}$ [see Eq. (9)] are neglected under WTG balance (Sobel et al. 2001), such that

$$\overline{\omega} = \frac{\overline{Q}_s - \dfrac{\partial \overline{\omega' s'}}{\partial p}}{\dfrac{\partial \overline{s}}{\partial p}}, \tag{13}$$

$$\frac{\partial \overline{h}}{\partial t} = L_v \frac{\partial \overline{q}}{\partial t}, \quad \text{and} \tag{14}$$

$$\overline{\mathbf{V}}_h \cdot \nabla \overline{h} = L_v \overline{\mathbf{V}}_h \cdot \nabla \overline{q}. \tag{15}$$

One method of assessing the applicability of WTG balance is to compare vertical velocity anomalies to those diagnosed using the right-hand side of Eq. (13). Figure 6a shows anomalous vertical velocity (color shading) and specific humidity (contours) throughout a composite convective life cycle of the MJO in the eastern Indian Ocean (5°N–10°S, 75°–85°E). Moving from the right side to the left side of the figure corresponds with the transition from suppressed convection to enhanced convection and back to suppressed convection, as indicated at the bottom of the figure. The largest specific humidity anomalies occur at 750 and 500 hPa, while the largest vertical velocity anomalies occur at around 400 hPa. Figure 6b shows the vertical velocity diagnosed using the right-hand side of Eq. (13), and Fig. 6c shows the difference between the actual and diagnosed vertical velocity. Please note that Q_1, which is used in the right-hand side of Eq. (13), was obtained directly from the ECMWF, not calculated as the sum of the Eulerian tendency and large-scale advective terms. While the right-hand side of Eq. (13) slightly underestimates vertical velocity anomalies below 200 hPa, and overestimates vertical velocity anomalies above 200 hPa, the evolution, vertical structure, and magnitude of the vertical velocity anomalies are well captured to first order. This suggests that a WTG balance framework is applicable to the MJO, consistent with the findings of previous studies (Chikira 2014; JZ). We wish to emphasize that this framework is not applicable within the boundary layer.

Assuming WTG balance and using Eqs. (13), (14), and (15), Eq. (12) becomes

$$\begin{aligned}\frac{\partial \overline{h}}{\partial t} = L_v \frac{\partial \overline{q}}{\partial t} &= -L_v \overline{\mathbf{V}}_h \cdot \nabla \overline{q} + \overline{\alpha}\left(\overline{Q}_s - \frac{\overline{\partial \omega' s'}}{\partial p}\right) \\ &\quad + L_v \overline{M} - L_v \frac{\partial \overline{\omega' q'}}{\partial p} \\ &= -L_v \overline{\mathbf{V}}_h \cdot \nabla \overline{q} + \overline{\alpha} Q_1 - Q_2, \end{aligned} \tag{16}$$

where

$$\overline{\alpha} = -L_v \left(\frac{\partial \overline{q}}{\partial p} \Big/ \frac{\partial \overline{s}}{\partial p} \right). \tag{17}$$

Note that $\overline{\alpha}$ (Chikira 2014) is essentially a measure of moisture sensitivity to apparent heating (Q_1). The variable $\overline{\alpha}$ is the quotient of the vertical moisture gradient and a measure of the static stability, with the latter determining the amount of vertical motion required to

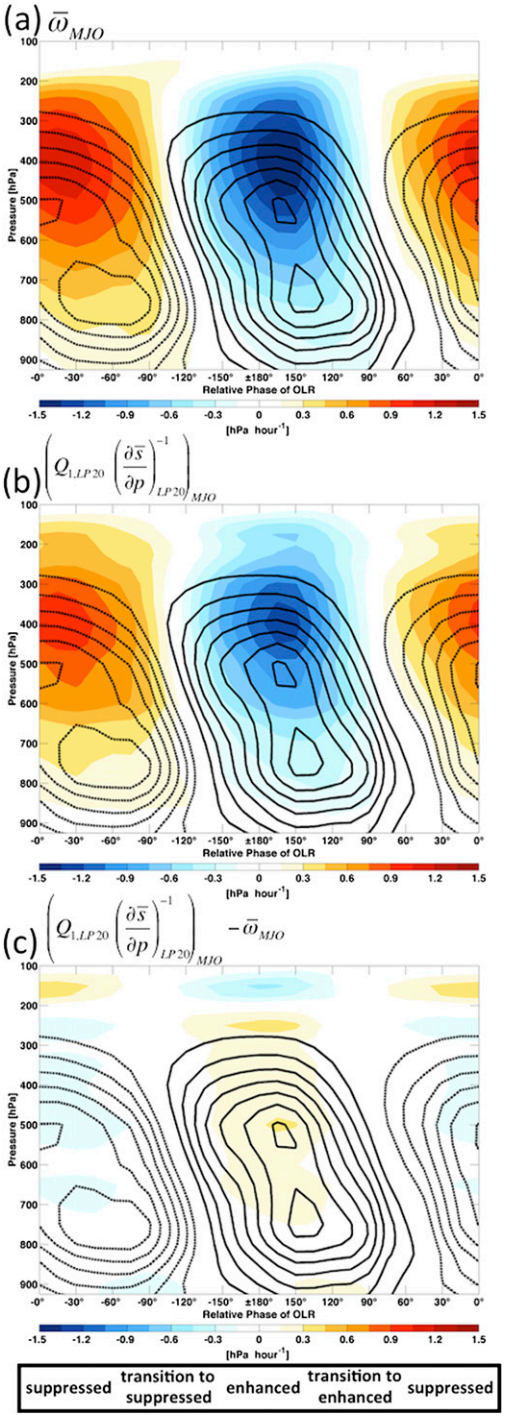

FIG. 6. Composite anomalies of vertical velocity (color shading) and specific humidity (contours) throughout a composite convective life cycle of the MJO in the eastern Indian Ocean (5°N–10°S, 75°–85°E). Solid (dashed) contours correspond to positive (negative) specific humidity anomalies every 0.1 g kg^{-1} beginning at ±0.1 g kg^{-1}. Moving from the right side to the left side of the figure corresponds with the transition from suppressed convection to enhanced convection and back to suppressed convection, as indicated at the bottom of the figure. The subscripts LP20 and MJO indicate application of 20-day lowpass and 20–100-day bandpass filtering, respectively. See text for description of compositing technique.

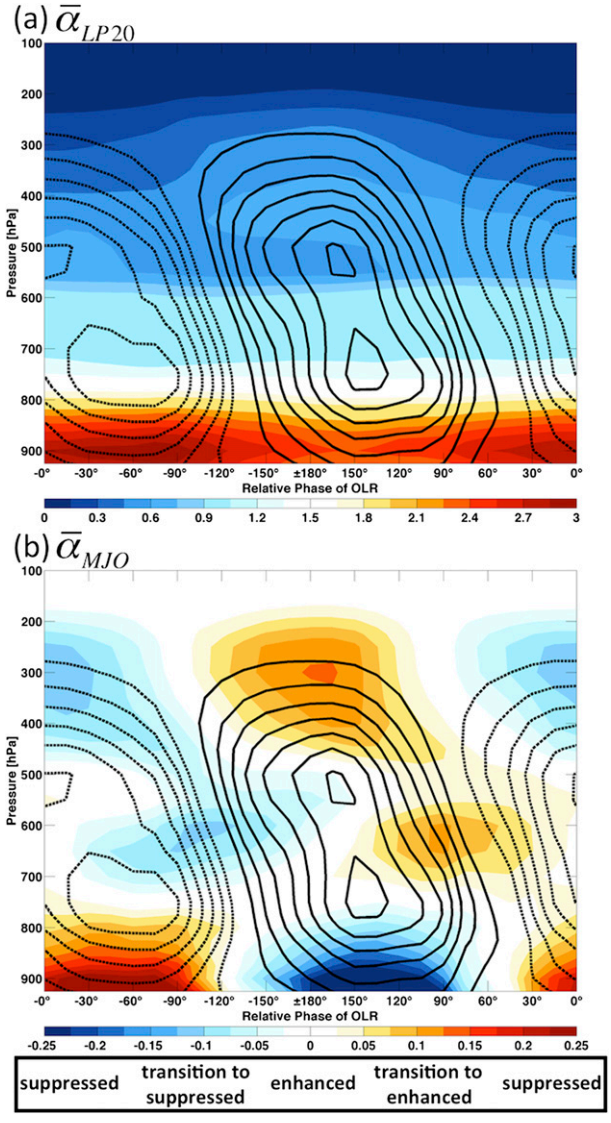

FIG. 7. As in Fig. 6, but color shading for $\overline{\alpha}$. The subscripts LP20 and MJO indicate application of 20-day lowpass and 20–100-day bandpass filtering, respectively.

balance an apparent heating and the former determining the amount of moistening that results from the required vertical motion. The vertical structure of α and anomalous α throughout a composite convective life cycle is shown in Figs. 7a,b, respectively. The lower troposphere has a particularly high moisture sensitivity to apparent heating, while the upper troposphere is relatively insensitive. Moistening of the lower and middle troposphere during the enhanced phase results in a reduction of α below 800 hPa and an increase of α above 400 hPa, consistent with the findings of Chikira (2014). The opposite is true during the suppressed phase.

To first order, moisture variations associated with intraseasonal variations in $\overline{\alpha}Q_1$ (Fig. 8b) result from intraseasonal variations in Q_1 (Fig. 8a) acting on the mean state $\overline{\alpha}$ profile (Fig. 9a). The mean state Q_1 profile acting on intraseasonal variations in $\overline{\alpha}$ (Fig. 9b) results in a much smaller moisture tendency, while intraseasonal variations in the Q_1 profile acting on intraseasonal variations in $\overline{\alpha}$ result in a negligible moisture tendency (not shown). Intraseasonal variations in Q_1 have a distinct peak in the upper troposphere, but the much larger values of $\overline{\alpha}$ in the lower troposphere result in a $\overline{\alpha}Q_1$ profile that is substantially more bottom heavy, with secondary peaks in moistening evident at 600 and 825 hPa. Intraseasonal variations in $Q_1 - \overline{Q}_R$ (Fig. 8c), which represents the apparent heating effect an ensemble cloud population has on its environment with the exclusion of radiative impacts (i.e., the net effect of microphysical processes and vertical eddy fluxes of DSE), account for much of the variation in Q_1. This heating drives moistening (Fig. 8d), which begins at the lowest levels of the troposphere during the suppressed phase, gradually increases in height during the transition to enhanced convection, and then makes an abrupt jump to the midlevels and finally upper levels during the enhanced phase. This stepwise pattern of moistening is reminiscent of that observed in the DYNAMO field campaign (Johnson and Ciesielski 2013). Note that the peak in midtropospheric moistening occurs prior to the largest midtropospheric moisture anomalies, and that drying is observed below 800 hPa throughout the enhanced phase. Intraseasonal variations in radiative heating (Fig. 8e), while smaller than intraseasonal variations in $Q_1 - \overline{Q}_R$, play an important role in determining the structure and magnitude of intraseasonal variations in apparent heating. The intraseasonal moisture tendency associated with radiative heating (Fig. 8f) is more bottom heavy than that which results from $Q_1 - \overline{Q}_R$, and is strongest slightly after the peak in midtropospheric moisture anomalies. This moistening, which counteracts the lower-tropospheric drying effects of $Q_1 - \overline{Q}_R$, may play a particularly important role in prolonging convection during the enhanced phase, as tropical convection is particularly sensitive to dry air entrainment below the freezing level (Lucas et al. 1994; Zipser 2003; Sahany et al. 2012).

Intraseasonal variations in both longwave and shortwave radiative heating (Figs. 10a,c) play an important role in determining the vertical structure and magnitude of $\overline{Q}_R$, though the longwave component is clearly dominant. Both longwave and shortwave radiative heating anomalies have vertical dipole structures that largely oppose each other, with the former being centered near 400 hPa with anomalous heating below this level during the enhanced phase, and the latter being centered near 550 hPa with anomalous cooling below this level during the enhanced phase. The vertical structure and magnitude of both longwave and shortwave radiative heating anomalies are comparable to those derived from *CloudSat*

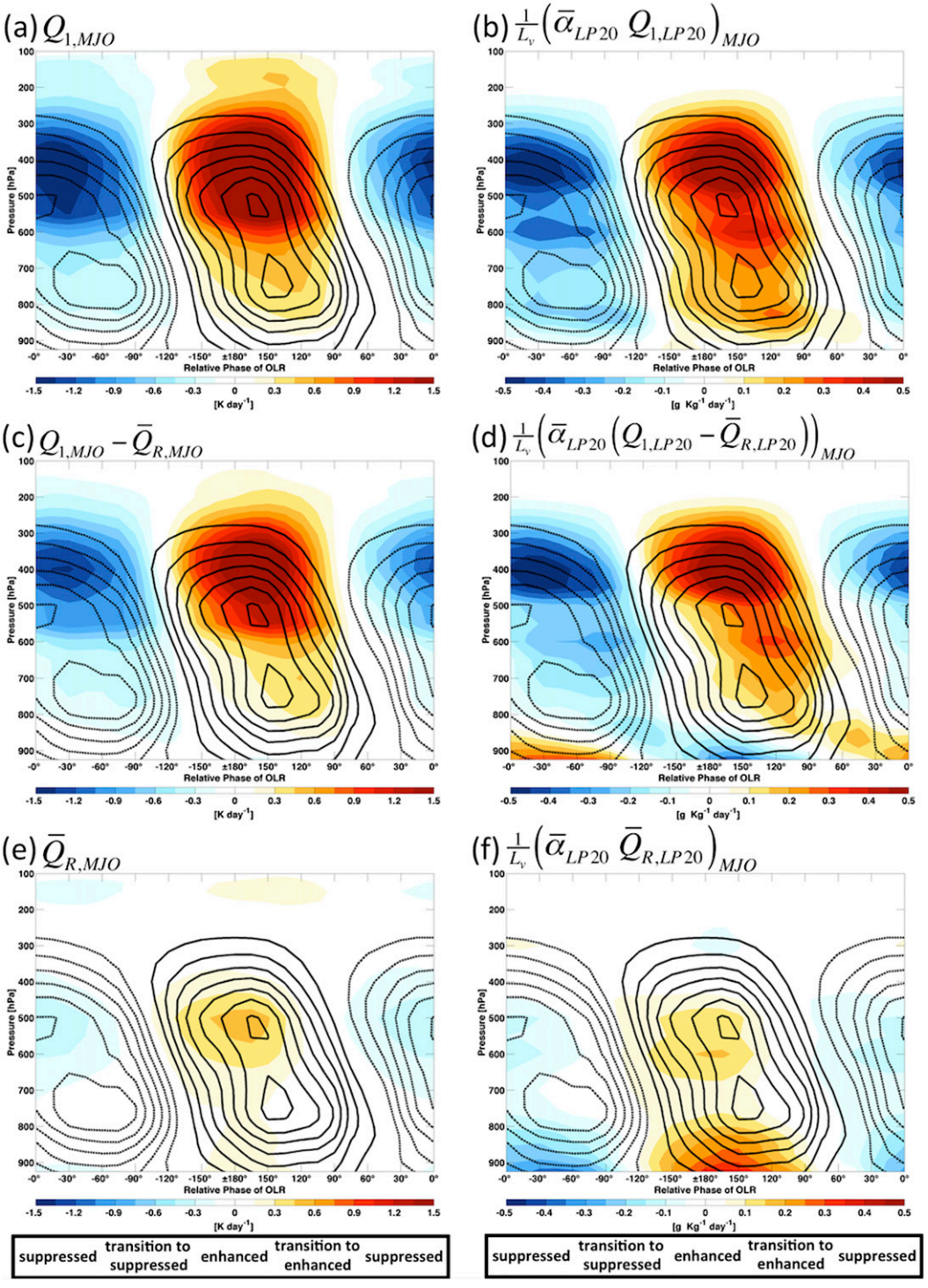

FIG. 8. As in Fig. 6, but color shading for various apparent heating terms and their associated moisture tendencies under weak temperature gradient balance. The subscripts LP20 and MJO indicate application of 20-day lowpass and 20–100-day bandpass filtering, respectively.

observations (Ma and Kuang 2011; Del Genio and Chen 2015), as is the phasing between radiative heating anomalies and moisture anomalies. Again, the vertical structure of $\overline{\alpha}$ is such that the profiles of the intraseasonal moisture tendencies associated with longwave and shortwave radiative heating (Figs. 10b,d) are substantially more bottom heavy than the anomalous radiative heating profiles, with the largest moisture tendencies occurring in the lower troposphere. During the enhanced phase, reduced longwave radiative cooling results in strong anomalous moistening in the lower and middle troposphere, while reduced shortwave heating results in anomalous drying, particularly below 750 hPa. When vertically integrated from 500 to 900 hPa (not shown), the latter is comparable with other moisture budget terms such as SLHF. While the effects of longwave radiative heating clearly dominate those of shortwave radiative heating, this result suggests the potential exists for interactions between the diurnal cycle and the MJO via radiative feedbacks. Further examination of this is beyond the scope of this study, and is left for future work.

Diagnosing variations in C_{free}, which represents the net effects of large-scale vertical moisture advection and microphysical processes within the free troposphere, is more complicated. Equation (16) can be rearranged and combined with Eq. (4) to give

$$C_{\text{free}} = \left\langle \frac{\overline{\alpha}}{L_v}\left(\overline{Q}_{\text{fm}} + \overline{Q}_R - \frac{\overline{\partial\omega' s'}}{\partial p}\right)\right\rangle_{900} + \left\langle \frac{\left(\overline{\alpha} - \frac{L_v}{L_s}\right)}{L_v}\overline{Q}_{\text{ds}}\right\rangle_{900} + \left\langle \frac{(\overline{\alpha}-1)}{L_v}\overline{Q}_{\text{ce}}\right\rangle_{900}$$
$$= \left\langle \frac{\overline{\alpha}}{L_v} Q_1\right\rangle_{900} + \langle \overline{M}\rangle_{900}. \tag{18}$$

Examination of Eq. (18) indicates that many different processes could potentially lead to an increase in C_{free}. An increase in net freezing, radiative heating, or vertical eddy fluxes of DSE would result in an increase in C_{free}. Net deposition and net condensation occurring where $\overline{\alpha}$ exceeds 0.8 and 1.0, respectively, would also result in an increase in C_{free}. In addition, the redistribution of any of these terms such that their vertical profiles became more bottom heavy would result in an increase in C_{free}. Unfortunately the limited output available from the ECMWF does not allow for the analysis of many of the individual terms in Eq. (18). Yet, as will be shown in a subsequent section, careful examination of the available terms allows important conclusions to be drawn about the changing character of C_{free} throughout the MJO life cycle.

In summary, application of a WTG balance framework to the MJO in the eastern Indian Ocean has allowed variations in large-scale vertical moisture advection within the free troposphere to be diagnosed from variations in apparent heating. Intraseasonal variations in large-scale vertical moisture advection within the free troposphere can, to first order, be understood as resulting from intraseasonal variations in apparent heating occurring in the mean state moist thermodynamic environment of the region. Anomalous radiative heating plays a dominant role in driving anomalous large-scale vertical advective moistening in the lower free troposphere during the enhanced phase, while the remaining apparent heating processes are the dominant drivers of anomalous large-scale vertical advective moistening in the middle and upper free troposphere. A reduction in shortwave radiative heating in the lower free troposphere during the enhanced phase results in anomalous large-scale vertical advective drying, partially opposing the anomalous large-scale vertical advective moistening that results from the reduction of longwave radiative cooling below 400 hPa. The vertically integrated MSE and moisture budgets will now be used to investigate variations in C and C_{free}.

3) Column MSE in WTG balance

In this section, the column MSE budget is used to assess the robustness of conclusions drawn in previous sections. Applying WTG balance [i.e., Eqs. (13)–(15)] above the boundary layer, and vertically integrating Eq. (12) through the depth of the troposphere gives

$$\frac{1}{L_v}\left(\left\langle\frac{\partial\overline{h}}{\partial t}\right\rangle - \left\langle\frac{\partial\overline{s}}{\partial t}\right\rangle_{1000}^{900}\right) = \left\langle\frac{\partial\overline{q}}{\partial t}\right\rangle = -\langle\overline{\mathbf{V}}_h\cdot\nabla\overline{q}\rangle + \langle C\rangle$$
$$= -\langle\overline{\mathbf{V}}_h\cdot\nabla\overline{q}\rangle + C_{\text{free}} + \text{BL} + \frac{1}{L_v}\overline{\text{SLHF}}. \tag{19}$$

As intraseasonal variations in the boundary layer DSE tendency are less than $1\,\mathrm{W\,m^{-2}}$ (not shown), negligible in comparison to other budget terms, Eq. (19) shows that under WTG balance the column MSE budget closely approximates the column moisture budget [Eq. (4)].

One benefit of the column moisture budget is that it offers a clean separation between moisture variations driven by surface fluxes of moisture (i.e., SLHF) and those driven by processes occurring within the atmospheric column. One benefit of deriving the column moisture budget from the MSE budget using a WTG balance framework is that it leads to Eq. (18), which provides insight to the physical mechanisms that can drive changes in C_{free}. A considerable disadvantage of using the moisture budget alone to investigate the MJO is the substantial budget residual (Fig. 5a) that, larger than several of the terms being investigated, brings into question the robustness of conclusions drawn from such an analysis. The residual appears to be due to the tendency of ERA-Interim to underestimate precipitation anomalies associated with the MJO when compared to observations, as recently observed during the DYNAMO field campaign (Sobel et al. 2014). Estimates of precipitation anomalies associated with the MJO based on ERA-Interim are systematically much less than those based on either TRMM or GPCP, which tend to agree fairly well (Morita et al. 2006; Benedict and Randall 2007; Lau and Wu 2010; Kiranmayi and Maloney 2011; Sobel et al. 2014; Kim et al. 2014b). This motivated the choice to calculate C as the residual of the moisture tendency and horizontal advection (Figs. 2e and 3e), and to calculate the sum of C_{free} and BL as the residual of the moisture tendency, horizontal advection, and SLHF (Figs. 2g and 3g). As MSE is conserved during condensation and evaporation, the MSE budget benefits from not needing to accurately quantify net condensation. This allows for approximate closure of the MSE budget, such that the MSE budget residual (Fig. 5b) is smaller than any term from which conclusions are drawn in this study.

The various terms of the MSE budget are presented in Fig. 11. Comparison of Figs. 3 and 11 shows that moisture anomalies account for approximately 90% of the MSE anomalies, and that WTG balance assumptions made in Eqs. (14) and (15) approximately hold. Under WTG balance, both the moisture budget and the MSE budget provide a similar assessment of the role of anomalous horizontal moisture advection and C anomalies (Figs. 3d,e and 11c,d, respectively) in the propagation and maintenance of moisture anomalies, providing confidence in conclusions drawn in earlier sections. Figures 11e,f show the sum of C_{free} and BL anomalies as assessed by the MSE budget, with and without inclusion of the budget residual, respectively. While the moisture budget suggests that the net effect of C_{free} and BL anomalies is to further grow moisture anomalies early in the enhanced phase (Fig. 3g), the MSE budget assessments provided in Figs. 11e,f suggest that the net effect of C_{free} and BL anomalies is to further enhance moisture anomalies later in the enhanced phase. It, therefore, remains uncertain whether the net effect of C_{free} and BL anomalies is to aid the growth of column moisture anomalies, support column moisture anomalies when they are largest, or slow the reduction

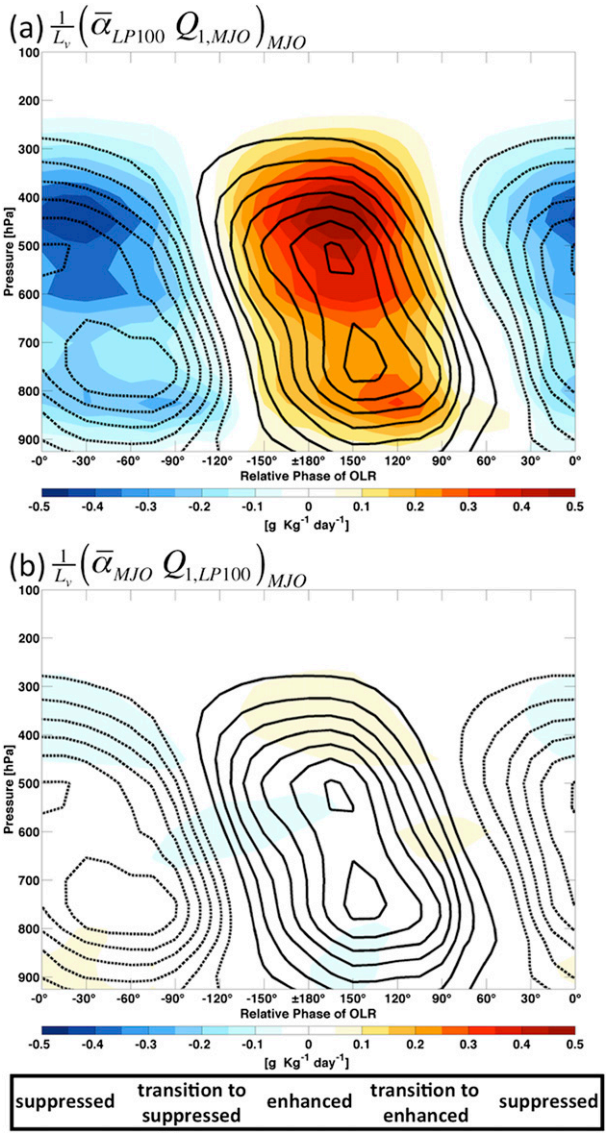

FIG. 9. As in Fig. 6, but color shading for the moisture tendency associated with various apparent heating terms under weak temperature gradient balance. The subscripts LP20, LP100, and MJO indicate application of 20-day lowpass, 100-day lowpass, and 20–100-day bandpass filtering, respectively.

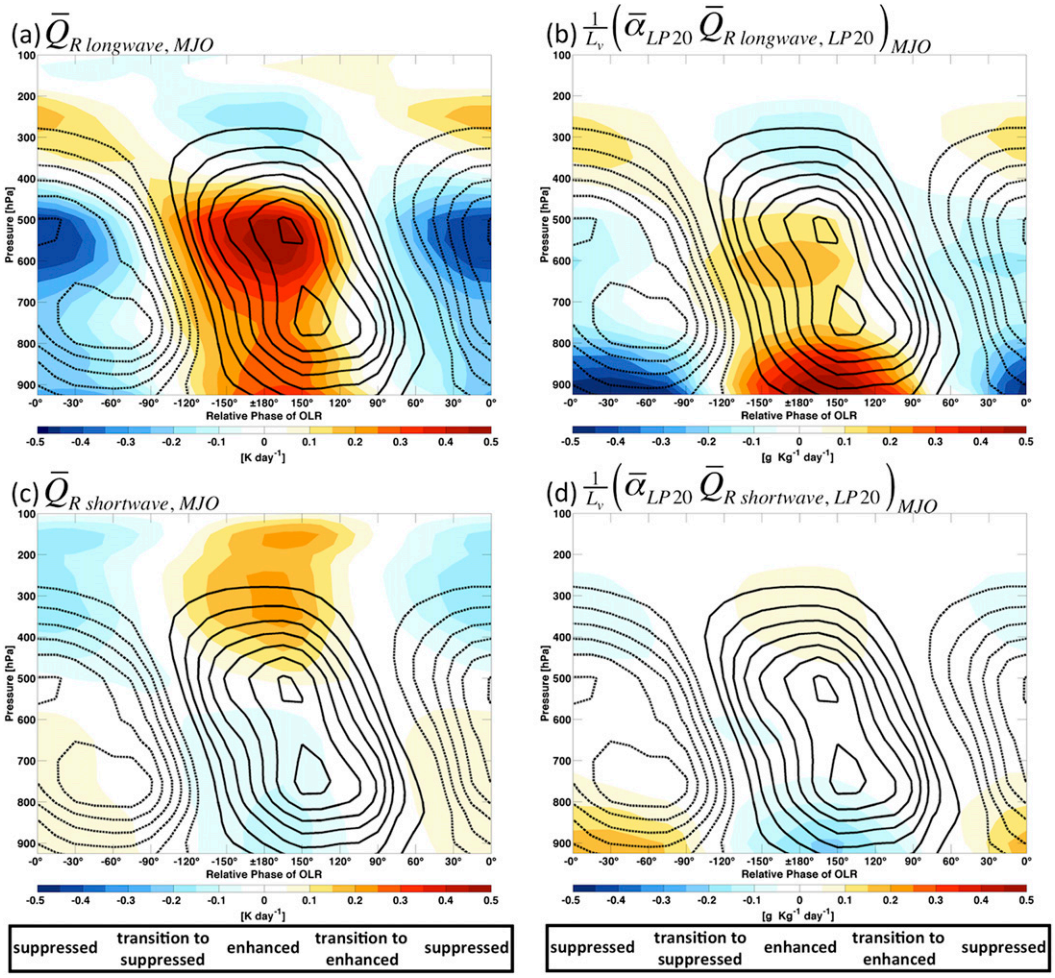

FIG. 10. As in Fig. 6, but color shading for (a) longwave and (c) shortwave radiative heating, and (b),(d) the associated moisture tendencies under weak temperature gradient balance. The subscripts LP20 and MJO indicate application of 20-day lowpass and 20–100-day bandpass filtering, respectively.

of column moisture anomalies. However, the moisture budget and MSE budget assessments are similar in that they suggest that the net effect of C_{free} and BL anomalies plays no role in ''discharging'' moisture anomalies during the enhanced phase, providing confidence that anomalous large-scale vertical moisture advection meets or exceeds anomalous moisture removal by microphysical processes throughout the enhanced phase.

In summary, it has been shown that, when interpreted using a WTG balance framework, the MSE budget supports the conclusions drawn in previous sections using the moisture budget. Foremost among these conclusions is that anomalous moistening by large-scale vertical moisture advection meets or exceeds anomalous drying by microphysical processes in the enhanced phase, and that anomalous drying by large-scale vertical moisture advection meets or exceeds the anomalous moistening by microphysical processes in the suppressed phase. The approximate closure of the MSE budget provides confidence that this conclusion is robust.

4) VARIATIONS IN THE COLUMN PROCESS AND THE IMPORTANCE OF RADIATIVE FEEDBACKS

Results presented in previous sections have shown that C anomalies act to enhance moisture anomalies where they are largest. The C anomalies result from variations in surface moisture fluxes, as well as large-scale vertical moisture advection and microphysical processes within both the boundary layer and free troposphere, given by the terms BL and C_{free}, respectively. As it is not possible to quantify C_{free} and BL individually given the data available from the ECMWF, their relative importance in destabilizing the MJO cannot be addressed. Yet careful examination of the available fields allows the effect of the changing ensemble cloud population on large-scale moisture to be assessed, and

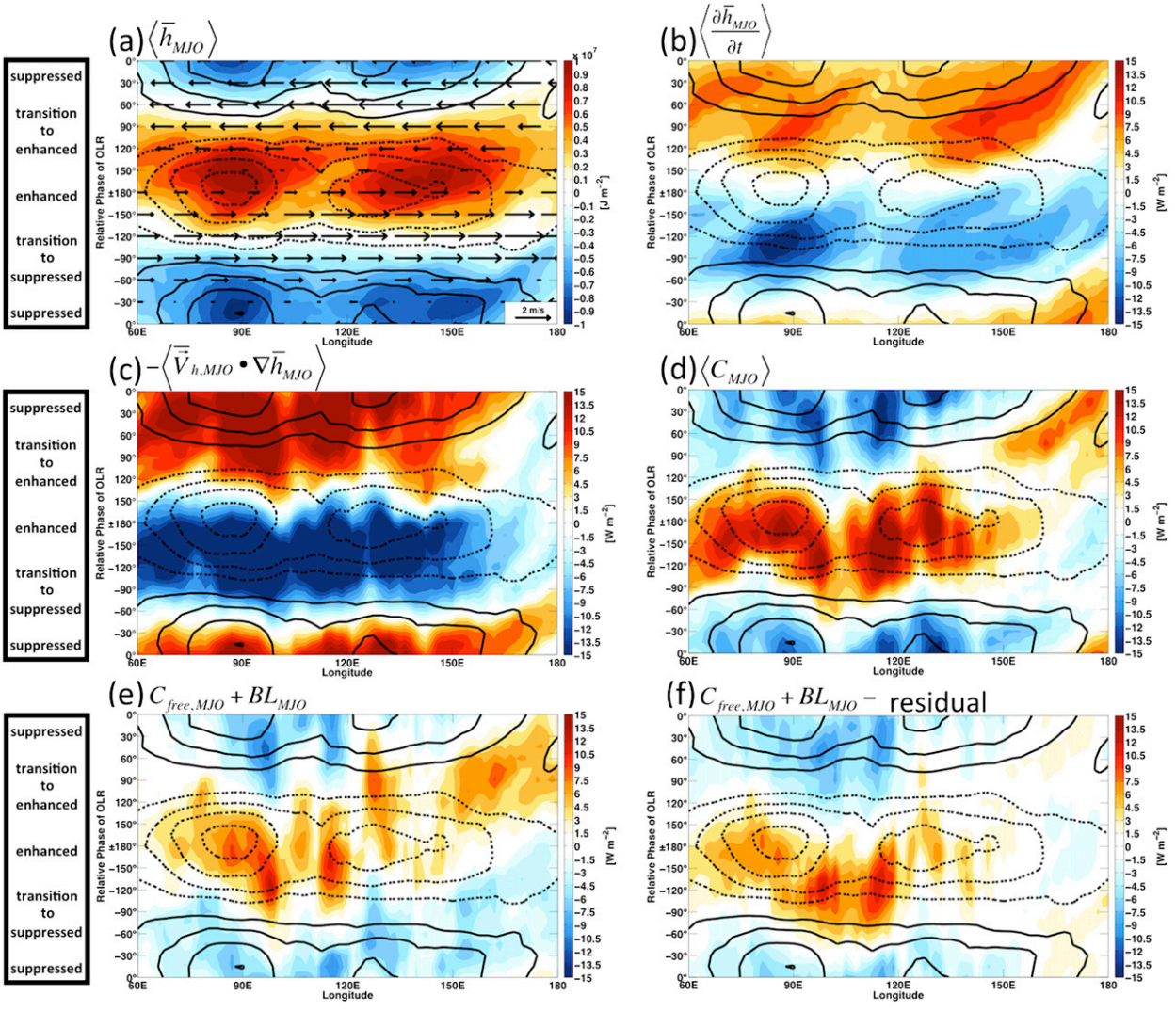

FIG. 11. As in Fig. 3, but color shading for anomalies of (a) column MSE, (b) column MSE tendency, (c) column horizontal advection of MSE, (d) column process, (e) the sum of C_{free} and BL, and (f) the sum of C_{free} and BL minus the MSE budget residual. The subscript MJO indicates bandpass filtering to 20–100 days.

the importance of radiative feedbacks to destabilizing the MJO to be addressed.

Examination of fields where only high-frequency variability (<20 days) has been removed provides insight to the effect of the changing ensemble cloud population on large-scale moisture, and how the ensemble cloud population may respond to an anomalous moisture source, such as enhanced SLHF or boundary layer moisture convergence. Before discussing Fig. 12, please note that each term has been vertically integrated from 900 to 100 hPa, the levels where WTG balance is applicable, and that only a 20-day low-pass filter has been applied. The numerators of the terms plotted in Figs. 12a–c are the latent heat variations associated with $\langle \overline{\alpha}(Q_1 - \overline{Q}_R) \rangle$, $\langle \overline{\alpha}\overline{Q}_R \rangle$, and $\langle \overline{\alpha} Q_1 \rangle$, respectively. To determine the amount of moisture resupplied by each of these terms per unit microphysical moisture loss, each term plotted in Fig. 12 has been normalized by $\langle Q_1 - \overline{Q}_R \rangle$. Intraseasonal variations in the Lagrangian tendency of specific ice water content were calculated (not shown) and found to be a negligible part of the MSE budget. Assuming little precipitation reaches the surface in the form of ice, this implies that $\langle Q_1 - \overline{Q}_R \rangle$ is approximately equal to net condensational heating of the column. In other words, each term in Fig. 12 is approximately normalized by net condensational heating of the column. Therefore Fig. 12 can be interpreted as the amount of moisture supplied by each

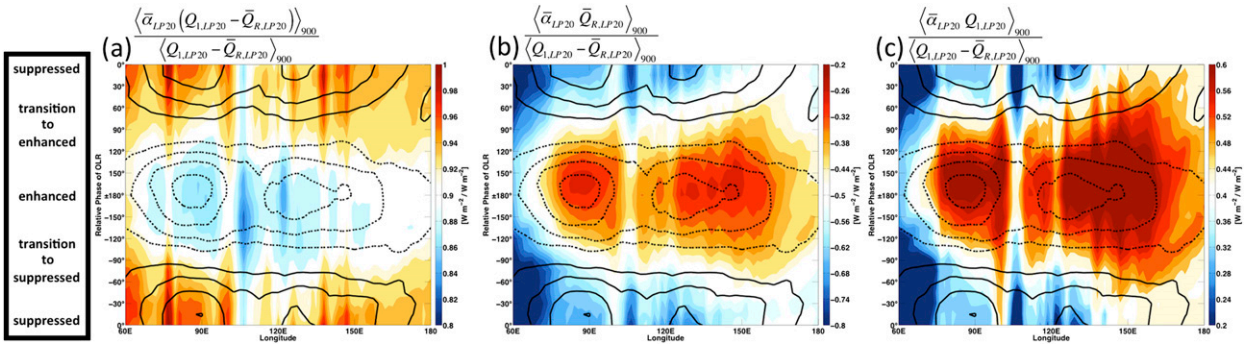

FIG. 12. As in Fig. 3, but color shading for the moisture tendency associated with various apparent heating terms under weak temperature gradient balance approximately normalized by net condensation. Please note that the vertical integral was only taken from 900 to 100 hPa with each of these terms, as weak temperature gradient balance is not applicable in the boundary layer. The subscripts LP20 and MJO indicate application of 20-day lowpass and 20–100-day bandpass filtering, respectively.

of these respective processes via large-scale vertical moisture advection per unit moisture loss due to net condensation.

Figure 12a shows the large-scale vertical moisture advection associated with apparent heating by microphysical processes and subgrid-scale DSE fluxes normalized by moisture loss due to net condensation; therefore, values less than 1 reflect a net drying of the column. Figure 12a shows that the net effect of $Q_1 - \overline{Q}_R$ is always to discharge moisture from the column, but to do so with surprising inefficiency. Remember that $Q_1 - \overline{Q}_R$ represents the apparent heating effect an ensemble cloud population has on its environment with the exclusion of radiative impacts. During the suppressed phase, more than 95% of the moisture lost by net condensation is resupplied by large-scale vertical moisture advection associated with $\langle \overline{\alpha}(Q_1 - \overline{Q}_R)\rangle$, while slightly less than 90% is resupplied during the enhanced phase. In other words, excluding its radiative impacts, the ensemble cloud population does become more efficient at discharging moisture from the environment during the enhanced phase, and less efficient at discharging moisture from the column during the suppressed phase, but these changes are relatively modest. The change in efficiency is driven by the progression from a bottom-heavy to top-heavy heating profile that occurs in the transition from suppressed to enhanced conditions. The remarkable inefficiency with which the net effects of an ensemble cloud population, excluding radiative impacts, remove moisture from the environment has important implications for the response of the cloud population to anomalous moisture sources. A disproportionately large increase in the net condensation produced by an ensemble cloud population would be required for the net effects of the ensemble cloud population, excluding radiative impacts, to remove an anomalous moisture source (e.g., enhanced SLHF). In other words, relatively small anomalous moisture sources could sustain relatively large increases in precipitation. Similar characteristics of the warm pool climatology were discussed by Sobel (2003).

This disproportionate response is exacerbated by the reduction of the large-scale vertical advective drying associated with radiative cooling that occurs when net condensation increases. Figure 12b shows that large-scale vertical advective drying associated with radiative cooling is always acting to dry the column more than the net effect of $Q_1 - \overline{Q}_R$ (Fig. 12a), even during the enhanced phase when radiative cooling is reduced and the $Q_1 - \overline{Q}_R$ profile becomes top heavy. In the mean state, the net effect an ensemble cloud population has on the large-scale environment (i.e., microphysical processes, radiative effects, and associated large-scale vertical advection) is always to remove moisture. Net condensation and the large-scale vertical advective drying associated with radiative cooling act together to remove moisture from the environment. But on intraseasonal time scales, an increase in net condensation is accompanied by a reduction in radiative cooling and associated large-scale vertical advective drying. The amount of drying associated with radiative cooling that occurs per unit net condensation changes dramatically throughout the MJO life cycle, varying from approximately 70% during the suppressed phase to approximately 20% during the enhanced phase (Fig. 12b). The result is that, per unit net condensation, approximately 3 times more moisture is resupplied by the large-scale vertical moisture advection associated with the total apparent heating of an ensemble cloud population and its radiative impacts during the enhanced phase than during the suppressed phase (Fig. 12c). The importance of these radiative feedbacks for destabilizing the MJO is now quantified.

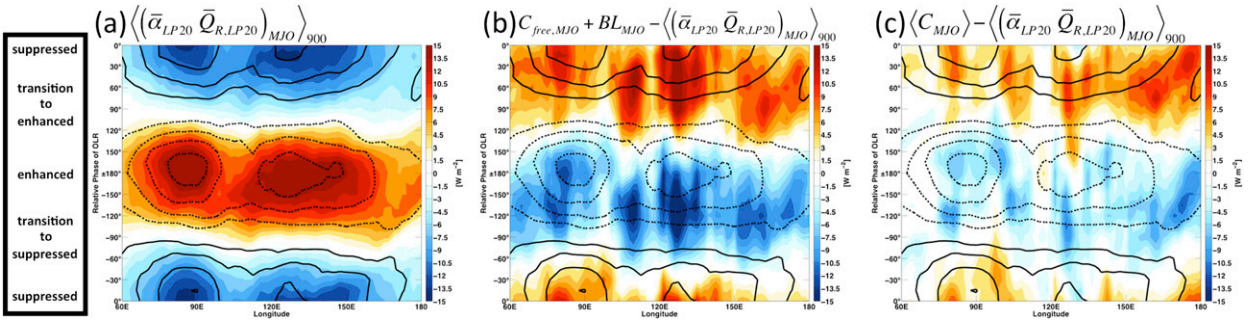

FIG. 13. As in Fig. 3, but color shading for (a) the intraseasonal moisture tendency associated with radiative heating, (b) the sum of C_{free} and BL minus the intraseasonal moisture tendency associated with radiative heating, and (c) the column process minus the intraseasonal moisture tendency associated with radiative heating. Please note that the vertical integral of the intraseasonal moisture tendency associated with radiative heating was only taken from 900 to 100 hPa, as the weak temperature gradient balance is not applicable in the boundary layer. The subscripts LP20 and MJO indicate application of 20-day lowpass and 20–100-day bandpass filtering, respectively.

Figure 13a shows intraseasonal variations in the column latent heat tendency associated with radiative heating anomalies above the boundary layer, which act as a strong positive feedback to moisture anomalies throughout the MJO life cycle. As shown in the previous section, these variations are largely the result of reduced longwave radiative cooling during the enhanced phase, and increased longwave radiative cooling during the suppressed phase. When these variations are subtracted from intraseasonal variations in the sum of C_{free} and BL (Fig. 13b), the net effect of microphysical processes, boundary layer moisture convergence, and the large-scale free-tropospheric vertical moisture advection associated with apparent heating by microphysical processes and subgrid-scale DSE fluxes is obtained. In other words, Fig. 13b shows the net effect boundary layer processes and the ensemble cloud population, excluding radiative impacts, have on large-scale moisture throughout the MJO life cycle. The effect is considerable drying during the later stages of the enhanced phase when stratiform precipitation is enhanced, and considerable moistening in the later stages of the suppressed phase when the proportion of shallow and congestus clouds are enhanced (Morita et al. 2006; Lau and Wu 2010; Riley et al. 2011). This is likely explained by the progression from a bottom-heavy to top-heavy heating profile that occurs in the transition from suppressed to enhanced conditions (Figs. 8c,d), and the relatively small values of $\overline{\alpha}$ in the upper troposphere. Figure 13b suggests that the net effect of C_{free} and BL would act to stabilize, not destabilize, the MJO if radiative feedbacks were not present. In fact, Fig. 13c suggests that the enhancement of SLHF during the enhanced phase would not be sufficient to overcome the anomalous drying effect that would result from the sum of C_{free} and BL if radiative feedbacks were not present. Given the small anomalous drying tendency observed during the enhanced phase in Fig. 13c, it seems plausible that the MJO could still be destabilized in an environment with relatively weak radiative feedbacks or relatively large variations in SLHF or boundary layer moisture convergence.

In summary, intraseasonal variations in radiative heating appear to play a crucial role in destabilizing the MJO, and have been shown to be essential in preventing the net effects of C_{free} and BL from reducing moisture anomalies. Throughout the MJO life cycle, apparent heating due to microphysical processes and subgrid-scale eddy fluxes of DSE is associated with large-scale vertical moisture advection that replaces most of the moisture removed by net condensation, suggesting that a disproportionately large convective response could be maintained by an anomalous moisture source or sink. While the apparent heating profile of the ensemble cloud population becomes more top heavy during the enhanced phase, and therefore produces less large-scale vertical moisture advection per unit apparent heating, the reduction of radiative cooling results in an increase in the ratio of apparent heating to net condensation. The net effect is that approximately 3 times more large-scale vertical moisture advection associated with the apparent heating of an ensemble cloud population is realized per unit net condensation during the enhanced phase than during the suppressed phase.

4. Conclusions

The anomalous MSE and moisture budgets of the MJO were investigated using 31 years of ERA-Interim data. The WTG balance is approximately satisfied, allowing the mechanisms controlling moisture variations associated with the MJO to be assessed using both MSE and moisture budgets. To first order, precipitation

anomalies are maintained by anomalous large-scale vertical moisture advection associated with the changing ensemble cloud population and its radiative effects. Composite analysis of the MJO in the eastern Indian Ocean clearly demonstrates that column process anomalies (i.e., the net effect of large-scale vertical moisture advection, microphysical processes, and SLHF) act to enhance column moisture anomalies in regions of increased precipitation. This enhancement of moisture anomalies results from an increase in SLHF, as well anomalous large-scale vertical moisture advection meeting or slightly exceeding the anomalous removal of moisture by microphysical processes. Increased SLHF appears to be insufficient to destabilize the MJO in the absence of radiative feedbacks, which play a crucial role in driving a positive feedback between column moisture anomalies and the net effects of anomalous large-scale vertical moisture advection and anomalous microphysical processes. The further enhancement of column moisture anomalies by column process anomalies is damped by anomalous horizontal moisture advection, which also acts to propagate the region of enhanced column moisture eastward. The geographical variability of these processes was investigated using objective methods developed in Part I of this study. The processes controlling moisture variations associated with the MJO in the eastern Indian Ocean are fairly representative of those occurring across the rest of the Indian Ocean, as well as oceanic regions of the Maritime Continent. The role of the various processes becomes less clear around the date line.

Application of a WTG balance framework to the MSE budget of the MJO has been used to provide insight into the physical mechanisms responsible for intraseasonal variations in large-scale vertical moisture advection within the free troposphere. To first order, intraseasonal variations in the magnitude and vertical structure of vertical velocity can be diagnosed from apparent heating. Intraseasonal variations in large-scale vertical moisture advection are largely explained by intraseasonal variations of apparent heating occurring in the mean state moist thermodynamic environment of a region. Anomalous apparent heating by microphysical processes and subgrid-scale eddy fluxes of DSE is associated with a stepwise pattern of moistening that begins in the lower troposphere during the suppressed phase, then transitions to the middle and finally upper troposphere in the enhanced phase, during which time anomalous drying is observed below 800 hPa. Anomalous moistening associated with anomalous radiative heating offsets this anomalous lower-tropospheric drying, and reenforces the moistening of the midtroposphere during the enhanced phase. In the column integral, this effect is strong enough to offset the anomalous drying by the net effect of microphysical processes and their associated large-scale vertical moisture advection.

Examination of vertical profiles of longwave and shortwave radiative heating anomalies provides a rich depiction of their respective roles in driving anomalous moisture tendencies, which cannot be gained by examining their column-integrated counterparts. During the enhanced phase, substantial lower- and midtropospheric moistening results from a reduction in longwave cooling below 400 hPa. This reduction of longwave radiative cooling plays a crucial role in the MJO, allowing anomalous large-scale vertical moisture advection to meet or exceed anomalous removal of moisture by microphysical processes, thereby driving a positive feedback between the net effect of these processes and moisture anomalies. Near-zero column shortwave heating anomalies result from a vertical dipole structure of anomalous heating and cooling that is centered near 550 hPa. Because of the high moisture sensitivity of the lower troposphere to apparent heating, the reduction of shortwave heating below 550 hPa during the enhanced phase is associated with anomalous drying that is comparable in magnitude to anomalous SLHF. While beyond the scope of this study, the importance of intraseasonal variations in shortwave radiative heating motivates further investigation into potential interactions between the diurnal cycle and the MJO via radiative feedbacks.

Changes in SLHF and horizontal moisture advection accompany changes in the ensemble cloud population. The results of this study suggest that disproportionately large changes in net condensation could be expected to result from changes in SLHF or horizontal moisture advection, as more than 85% of the moisture removed by net condensation during the enhanced phase is resupplied by the large-scale vertical moisture advection associated with microphysical processes and subgrid-scale eddy fluxes of DSE. It is worth reiterating that this disproportionate response would act to remove moisture anomalies in the absence of radiative feedbacks, which appear to play an essential role in destabilizing the MJO. The increase of horizontal advective drying appears to be the only process damping the further growth of moisture anomalies during the latter portions of the enhanced phase.

Discharge–recharge theory, moisture-mode theory, and destabilization of the MJO

Discharge–recharge theory and moisture-mode theory are compatible in many ways. Yet it is generally understood, if not explicitly stated, that suppressed

convective conditions play a destabilizing role, and enhanced convective conditions a stabilizing role, in discharge–recharge theory, while both conditions play a destabilizing role in moisture-mode theory. The results of this study highlight that the distinction between the two can be incredibly fine.

It has been shown that when radiative feedbacks are excluded, column process anomalies have a weak stabilizing effect on the MJO. This result suggests that MJO-like variability with the characteristics of a ''discharge–recharge'' phenomena may be produced in an environment with relatively weak radiative feedbacks or relatively strong SLHF anomalies. This may be how MJO-like variability is maintained in some model simulations (Maloney et al. 2010), and helps to explain the wide-ranging results of mechanism denial experiments. Yet the results of this study, as well as the results of Chikira (2014) and JZ, suggest that strong radiative feedbacks are a fundamental feature of the MJO, and that the characteristics of the MJO are those of a moisture-mode phenomena. What criteria should be considered when assessing how ''MJO-like'' model variability is? Is it sufficient to have a large-scale coupling of deep convection and tropospheric circulation anomalies that propagates eastward at approximately $5\,m\,s^{-1}$? Or should a realistic destabilization mechanism also be a prerequisite to be considered MJO-like variability?

The results of this study paint a picture of the MJO as a persistent, but somewhat ''glass jaw'' phenomenon. Persistent in that a positive feedback between column moisture anomalies and the net effects of an ensemble cloud population appear to systematically push environmental conditions in the Indian Ocean and oceanic regions of the Maritime Continent toward extremes of enhanced or suppressed convection during periods of MJO activity. Glass jaw in that this positive feedback appears to be fairly modest, easily overcome by transient events such as dry air intrusions from the subtropics. Foremost among the shortcomings of this paper is the inability to systematically address the role of boundary layer processes, which have been shown to be important on intraseasonal time scales (DeMott et al. 2014). Further investigation into the role various microphysical processes play in modifying the vertical structure and magnitude of apparent heating throughout the MJO life cycle is needed. As only a single reanalysis product was implemented in this study, the robustness of conclusions presented here should be tested using other observational, reanalysis, and modeling products.

Acknowledgments. We are very grateful for the valuable comments of the two anonymous reviewers. Many thanks to Thomas Birner for acquiring and generously sharing much of the data used in this study. The careful reading and insightful comments of George Kiladis greatly improved this manuscript. Interpolated OLR data were provided by the NOAA/OAR/ESRL PSD, Boulder, Colorado, from their website (http://www.esrl.noaa.gov/psd/). The ERA-Interim data were obtained from the ECMWF data server. This work was supported by the NOAA ESS program under Grant NA13OAR4310163, the Climate and Large-Scale Dynamics Program of the National Science Foundation under Grant AGS-1062161, and the Science and Technology Center for Multiscale Modeling of Atmospheric Processes (CMMAP), managed by the Colorado State University under Cooperative Agreement ATM-0425247. The statements, findings, conclusions, and recommendations do not necessarily reflect the views of NOAA, NSF, or CMMAP.

REFERENCES

Andersen, J. A., and Z. Kuang, 2012: Moist static energy budget of MJO-like disturbances in the atmosphere of a zonally symmetric aquaplanet. *J. Climate*, **25**, 2782–2804, doi:10.1175/JCLI-D-11-00168.1.

Benedict, J. J., and D. A. Randall, 2007: Observed characteristics of the MJO relative to maximum rainfall. *J. Atmos. Sci.*, **64**, 2332–2354, doi:10.1175/JAS3968.1.

Bladé, I., and D. L. Hartmann, 1993: Tropical intraseasonal oscillations in a simple nonlinear model. *J. Atmos. Sci.*, **50**, 2922–2939, doi:10.1175/1520-0469(1993)050<2922:TIOIAS>2.0.CO;2.

Charney, J. G., 1963: A note on large-scale motions in the tropics. *J. Atmos. Sci.*, **20**, 607–609, doi:10.1175/1520-0469(1963)020<0607:ANOLSM>2.0.CO;2.

Chikira, M., 2014: Eastward-propagating intraseasonal oscillation represented by Chikira–Sugiyama cumulus parameterization. Part II: Understanding moisture variation under weak temperature gradient balance. *J. Atmos. Sci.*, **71**, 615–639, doi:10.1175/JAS-D-13-038.1.

Dee, D., and Coauthors, 2011: The ERA-Interim reanalysis: Configuration and performance of the data assimilation system. *Quart. J. Roy. Meteor. Soc.*, **137**, 553–597, doi:10.1002/qj.828.

Del Genio, A. D., and Y. Chen, 2015: Cloud-radiative driving of the Madden-Julian oscillation as seen by the A-Train. *J. Geophys. Res. Atmos.*, **120**, 5344–5356, doi:10.1002/2015JD023278.

DeMott, C. A., C. Stan, D. A. Randall, and M. D. Branson, 2014: Intraseasonal variability in coupled GCMs: The roles of ocean feedbacks and model physics. *J. Climate*, **27**, 4970–4995, doi:10.1175/JCLI-D-13-00760.1.

Hall, J. D., A. J. Matthews, and D. J. Karoly, 2001: The modulation of tropical cyclone activity in the Australian region by the Madden–Julian oscillation. *Mon. Wea. Rev.*, **129**, 2970–2982, doi:10.1175/1520-0493(2001)129<2970:TMOTCA>2.0.CO;2.

Hu, Q., and D. A. Randall, 1994: Low-frequency oscillations in radiative-convective systems. *J. Atmos. Sci.*, **51**, 1089–1099, doi:10.1175/1520-0469(1994)051<1089:LFOIRC>2.0.CO;2.

Johnson, R., and P. Ciesielski, 2013: Evolution of MJO convection during DYNAMO deduced from the atmospheric sounding network. *EGU General Assembly Conference Abstracts*,

Vol. 15, Abstract 2115. [Abstract available online at http://adsabs.harvard.edu/abs/2013EGUGA..15.2115.]

Kemball-Cook, S. R., and B. C. Weare, 2001: The onset of convection in the Madden-Julian oscillation. *J. Climate*, **14**, 780–793, doi:10.1175/1520-0442(2001)014<0780:TOOCIT>2.0.CO;2.

Kiladis, G. N., K. H. Straub, and P. T. Haertel, 2005: Zonal and vertical structure of the Madden–Julian oscillation. *J. Atmos. Sci.*, **62**, 2790–2809, doi:10.1175/JAS3520.1.

——, J. Dias, K. H. Straub, M. C. Wheeler, S. N. Tulich, K. Kikuchi, K. M. Weickmann, and M. J. Ventrice, 2014: A comparison of OLR and circulation-based indices for tracking the MJO. *Mon. Wea. Rev.*, **142**, 1697–1715, doi:10.1175/MWR-D-13-00301.1.

Kim, D., J.-S. Kug, and A. H. Sobel, 2014a: Propagating versus nonpropagating Madden–Julian oscillation events. *J. Climate*, **27**, 111–125, doi:10.1175/JCLI-D-13-00084.1.

——, M.-I. Lee, D. Kim, S. D. Schubert, D. E. Waliser, and B. Tian, 2014b: Representation of tropical subseasonal variability of precipitation in global reanalyses. *Climate Dyn.*, **43**, 517–534, doi:10.1007/s00382-013-1890-x.

Kiranmayi, L., and E. D. Maloney, 2011: Intraseasonal moist static energy budget in reanalysis data. *J. Geophys. Res.*, **116**, D21117, doi:10.1029/2011JD016031.

Lau, K., and H. Wu, 2010: Characteristics of precipitation, cloud, and latent heating associated with the Madden–Julian oscillation. *J. Climate*, **23**, 504–518, doi:10.1175/2009JCLI2920.1.

Liebmann, B., and C. Smith, 1996: Description of a complete (interpolated) outgoing longwave radiation dataset. *Bull. Amer. Meteor. Soc.*, **77**, 1275–1277.

Ling, J., C. Zhang, and P. Bechtold, 2013: Large-scale distinctions between MJO and non-MJO convective initiation over the tropical Indian Ocean. *J. Atmos. Sci.*, **70**, 2696–2712, doi:10.1175/JAS-D-13-029.1.

Lucas, C., E. J. Zipser, and M. A. Lemone, 1994: Vertical velocity in oceanic convection off tropical Australia. *J. Atmos. Sci.*, **51**, 3183–3193, doi:10.1175/1520-0469(1994)051<3183:VVIOCO>2.0.CO;2.

Ma, D., and Z. Kuang, 2011: Modulation of radiative heating by the Madden–Julian Oscillation and convectively coupled Kelvin waves as observed by *CloudSat*. *Geophys. Res. Lett.*, **38**, L21813, doi:10.1029/2011GL049734.

Madden, R. A., and P. R. Julian, 1971: Detection of a 40-50 day oscillation in the zonal wind in the tropical Pacific. *J. Atmos. Sci.*, **28**, 702–708, doi:10.1175/1520-0469(1971)028<0702:DOADOI>2.0.CO;2.

——, and ——, 1972: Description of global-scale circulation cells in the tropics with a 40-50 day period. *J. Atmos. Sci.*, **29**, 1109–1123, doi:10.1175/1520-0469(1972)029<1109:DOGSCC>2.0.CO;2.

Majda, A. J., and S. N. Stechmann, 2009: The skeleton of tropical intraseasonal oscillations. *Proc. Natl. Acad. Sci. USA*, **106**, 8417–8422, doi:10.1073/pnas.0903367106.

——, and ——, 2011: Nonlinear dynamics and regional variations in the MJO skeleton. *J. Atmos. Sci.*, **68**, 3053–3071, doi:10.1175/JAS-D-11-053.1.

Maloney, E. D., 2009: The moist static energy budget of a composite tropical intraseasonal oscillation in a climate model. *J. Climate*, **22**, 711–729, doi:10.1175/2008JCLI2542.1.

——, and D. L. Hartmann, 2000a: Modulation of eastern North Pacific hurricanes by the Madden–Julian oscillation. *J. Climate*, **13**, 1451–1460, doi:10.1175/1520-0442(2000)013<1451:MOENPH>2.0.CO;2.

——, and ——, 2000b: Modulation of hurricane activity in the Gulf of Mexico by the Madden–Julian oscillation. *Science*, **287**, 2002–2004, doi:10.1126/science.287.5460.2002.

——, and A. H. Sobel, 2007: Idealized hot spot experiments with a general circulation model. *J. Climate*, **20**, 908–925, doi:10.1175/JCLI4053.1.

——, ——, and W. M. Hannah, 2010: Intraseasonal variability in an aquaplanet general circulation model. *J. Adv. Model. Earth Syst.*, **2** (5), doi:10.3894/JAMES.2010.2.5.

Matthews, A. J., 2008: Primary and successive events in the Madden–Julian oscillation. *Quart. J. Roy. Meteor. Soc.*, **134**, 439–453, doi:10.1002/qj.224.

McPhaden, M. J., 1999: Genesis and evolution of the 1997-98 El Niño. *Science*, **283**, 950–954, doi:10.1126/science.283.5404.950.

Morita, J., Y. N. Takayabu, S. Shige, and Y. Kodama, 2006: Analysis of rainfall characteristics of the Madden–Julian oscillation using TRMM satellite data. *Dyn. Atmos. Oceans*, **42**, 107–126, doi:10.1016/j.dynatmoce.2006.02.002.

Neelin, J. D., O. Peters, and K. Hales, 2009: The transition to strong convection. *J. Atmos. Sci.*, **66**, 2367–2384, doi:10.1175/2009JAS2962.1.

Peters, O., and J. D. Neelin, 2006: Critical phenomena in atmospheric precipitation. *Nat. Phys.*, **2**, 393–396, doi:10.1038/nphys314.

Pritchard, M. S., and C. S. Bretherton, 2014: Causal evidence that rotational moisture advection is critical to the superparameterized Madden–Julian oscillation. *J. Atmos. Sci.*, **71**, 800–815, doi:10.1175/JAS-D-13-0119.1.

Raymond, D. J., 1995: Regulation of moist convection over the west Pacific warm pool. *J. Atmos. Sci.*, **52**, 3945–3959, doi:10.1175/1520-0469(1995)052<3945:ROMCOT>2.0.CO;2.

——, 2001: A new model of the Madden-Julian oscillation. *J. Atmos. Sci.*, **58**, 2807–2819, doi:10.1175/1520-0469(2001)058<2807:ANMOTM>2.0.CO;2.

——, and Ž. Fuchs, 2009: Moisture modes and the Madden–Julian oscillation. *J. Climate*, **22**, 3031–3046, doi:10.1175/2008JCLI2739.1.

Riley-Dellaripa, E. M., and E. D. Maloney, 2015: Analysis of MJO wind-flux feedbacks in the Indian Ocean using RAMA buoy observations. *J. Meteor. Soc. Japan*, doi:10.2151/jmsj.2015-021, in press.

——, B. E. Mapes, and S. N. Tulich, 2011: Clouds associated with the Madden–Julian oscillation: A new perspective from *CloudSat*. *J. Atmos. Sci.*, **68**, 3032–3051, doi:10.1175/JAS-D-11-030.1.

Sahany, S., J. D. Neelin, K. Hales, and R. B. Neale, 2012: Temperature-moisture dependence of the deep convective transition as a constraint on entrainment in climate models. *J. Atmos. Sci.*, **69**, 1340–1358, doi:10.1175/JAS-D-11-0164.1.

Shinoda, T., H. H. Hendon, and J. Glick, 1998: Intraseasonal variability of surface fluxes and sea surface temperature in the tropical western Pacific and Indian Oceans. *J. Climate*, **11**, 1685–1702, doi:10.1175/1520-0442(1998)011<1685:IVOSFA>2.0.CO;2.

Slade, S. A., and E. D. Maloney, 2013: An intraseasonal prediction model of Atlantic and east Pacific tropical cyclone genesis. *Mon. Wea. Rev.*, **141**, 1925–1942, doi:10.1175/MWR-D-12-00268.1.

Sobel, A. H., 2003: On the coexistence of an evaporation minimum and precipitation maximum in the warm pool. *J. Climate*, **16**, 1003–1009, doi:10.1175/1520-0442(2003)016<1003:OTCOAE>2.0.CO;2.

——, and E. Maloney, 2012: An idealized semi-empirical framework for modeling the Madden–Julian oscillation. *J. Atmos. Sci.*, **69**, 1691–1705, doi:10.1175/JAS-D-11-0118.1.

——, and ——, 2013: Moisture modes and the eastward propagation of the MJO. *J. Atmos. Sci.*, **70**, 187–192, doi:10.1175/JAS-D-12-0189.1.

——, J. Nilsson, and L. M. Polvani, 2001: The weak temperature gradient approximation and balanced tropical moisture waves. *J. Atmos. Sci.*, **58**, 3650–3665, doi:10.1175/1520-0469(2001)058<3650:TWTGAA>2.0.CO;2.

——, S. Wang, and D. Kim, 2014: Moist static energy budget of the MJO during DYNAMO. *J. Atmos. Sci.*, **71**, 4276–4291, doi:10.1175/JAS-D-14-0052.1.

Takayabu, Y. N., T. Iguchi, M. Kachi, A. Shibata, and H. Kanzawa, 1999: Abrupt termination of the 1997–98 El Niño in response to a Madden–Julian oscillation. *Nature*, **402**, 279–282, doi:10.1038/46254.

Thayer-Calder, K., and D. A. Randall, 2009: The role of convective moistening in the Madden–Julian oscillation. *J. Atmos. Sci.*, **66**, 3297–3312, doi:10.1175/2009JAS3081.1.

Wang, B., 2012: Theories. *Intraseasonal Variability in the Atmosphere-Ocean Climate System*, 2nd ed. W. K. M. Lau and D. E. Waliser, Eds., Springer, 335–398.

Wheeler, M. C., and H. H. Hendon, 2004: An all-season real-time multivariate MJO index: Development of an index for monitoring and prediction. *Mon. Wea. Rev.*, **132**, 1917–1932, doi:10.1175/1520-0493(2004)132<1917:AARMMI>2.0.CO;2.

Wolding, B. O., and E. D. Maloney, 2015: Objective diagnostics and the Madden–Julian oscillation. Part I: Methodology. *J. Climate*, **28**, 4127–4140, doi:10.1175/JCLI-D-14-00688.1.

Wu, X., and L. Deng, 2013: Comparison of moist static energy and budget between the GCM-simulated Madden–Julian oscillation and observations over the Indian Ocean and western Pacific. *J. Climate*, **26**, 4981–4993, doi:10.1175/JCLI-D-12-00607.1.

Yanai, M., and R. Johnson, 1993: Impacts of cumulus convection on thermodynamic fields. *The Representation of Cumulus Convection in Numerical Models, Meteor. Monogr.*, No. 24, Amer. Meteor. Soc., 39–62.

——, S. Esbensen, and J.-H. Chu, 1973: Determination of bulk properties of tropical cloud clusters from large-scale heat and moisture budgets. *J. Atmos. Sci.*, **30**, 611–627, doi:10.1175/1520-0469(1973)030<0611:DOBPOT>2.0.CO;2.

Yano, J.-I., and M. Bonazzola, 2009: Scale analysis for large-scale tropical atmospheric dynamics. *J. Atmos. Sci.*, **66**, 159–172, doi:10.1175/2008JAS2687.1.

Yokoi, S., 2015: Multireanalysis comparison of variability in column water vapor and its analysis increment associated with the Madden–Julian oscillation. *J. Climate*, **28**, 793–808, doi:10.1175/JCLI-D-14-00465.1.

Zhang, C., 2005: Madden–Julian oscillation. *Rev. Geophys.*, **43**, RG2003, doi:10.1029/2004RG000158.

Zipser, E. J., 2003: Some views on ''hot towers'' after 50 years of tropical field programs and two years of TRMM data. *Cloud Systems, Hurricanes, and the Tropical Rainfall Measuring Mission (TRMM), Meteor. Monogr.*, No. 29, Amer. Meteor. Soc., 49–58, doi:10.1175/0065-9401(2003)029<0049:CSVOHT>2.0.CO;2.